## Title

Dual carbonate clumped isotopes (Δ47-Δ48) constrains kinetic effects and timescales in peridotite-associated springs at the Cedars, Northern California



## Authors

Parvez, Zeeshan A
Lucarelli, Jamie K
Matamoros, Irvin W
et al.

## Publication Date

2023-10-01

## DOI

10.1016/j.gca.2023.06.022

# Dual carbonate clumped isotopes ($\Delta_{47}$-$\Delta_{48}$) constrains kinetic effects and timescales in peridotite-associated springs at The Cedars, Northern California

Zeeshan A. Parvez[a, b, c,*], Jamie K. Lucarelli[a,b,*], Irvin W. Matamoros[a, b], Joshua Rubi[b, d], Kevin Miguel[b, d], Ben Elliott[a, b], Randy Flores[a, b], Robert N. Ulrich[a, b], Robert A. Eagle[b, e, f], James M. Watkins[g], John N. Christensen[h], Aradhna Tripati[a, b, e, f]

[a] *Department of Earth, Planetary, and Space Sciences, University of California, Los Angeles, CA, USA*
[b] *Center for Diversity and Leadership in Science, University of California, Los Angeles, CA, USA*
[c] *Department of Chemistry and Biochemistry, University of California, Los Angeles, CA, USA*
[d] *East Los Angeles College, Los Angeles, CA, USA*
[e] *Department of Atmospheric and Oceanic Sciences, University of California, Los Angeles, CA, USA*
[f] *Institute of Environment and Sustainability, University of California, Los Angeles, CA, USA*
[g] *Department of Earth Sciences, University of Oregon, Eugene, OR, USA*
[h] *Department of Energy Geosciences, Lawrence Berkeley National Laboratory, Berkeley CA, USA*

* *Joint first author.*

Corresponding author: Aradhna Tripati, atripati@g.ucla.edu

## Abstract

The Cedars is an area in Northern California with a chain of highly alkaline springs resulting from $CO_2$-charged meteorological water interacting with a peridotite body. Serpentinization resulting from this interaction at depth leads to the sequestration of various carbonate minerals into veins accompanied by a release of $Ca^{2+}$ and $OH^-$ enriched water to the surface, creating an environment which promotes rapid precipitation of $CaCO_3$ at surface springs. This environment enables us to apply the recently developed $\Delta_{47}$-$\Delta_{48}$ dual clumped isotope analysis to probe kinetic isotope effects (KIEs) and timescales of $CO_2$ transformation in a region with the potential for geological $CO_2$ sequestration. We analyzed $CaCO_3$ recovered from various localities and identified significant kinetic fractionations associated with $CO_2$ absorption in a majority of samples, characterized by enrichment in $\Delta_{47}$ values and depletion in $\Delta_{48}$ values relative to equilibrium. Surface floes exhibited the largest KIEs ($\Delta\Delta_{47}$: 0.163‰, $\Delta\Delta_{48}$: -0.761‰). Surface floe samples begin to precipitate out of solution within the first hour of $CO_2$ absorption, and the dissolved inorganic carbon (DIC) pool requires a residence time of >100 hours to achieve isotopic equilibria. The $\Delta_{48}/\Delta_{47}$ slope of samples from the Cedars (-3.223±0.519) is within the range of published theoretical values designed to constrain $CO_2$ hydrolysis-related kinetic fractionation (-1.724 to -8.330). The $\Delta_{47}/\delta^{18}O$ slope (-0.009±0.001) and $\Delta_{47}/\delta^{13}C$ slope (0.009±0.001) are roughly consistent with literature values reported from a peridotite in Oman of -0.006±0.002 and -0.005±0.002, respectively. The consistency of slopes in the multi-isotope space suggests the $\Delta_{47}$-$\Delta_{48}$ dual carbonate clumped isotope framework can be applied to study $CO_2$-absorption processes in applied systems, including sites of interest for geological sequestration.

## 1. Introduction

The rate and mechanism of $CO_2$ transformation into carbonate minerals in natural alkaline springs and peridotites is of interest because of the potential for permanent, non-toxic $CO_2$ sequestration. Carbon mineralization at peridotites that host alkaline springs exist worldwide. It is hypothesized that serpentinization, a process that involves the hydration of ultramafic minerals, facilitates the carbon mineralization process in peridotite bodies (Bruni et al., 2002; Falk et al., 2016; García del Real et al., 2016; Suzuki et al., 2017; de Obeso and Kelemen, 2018). Serpentinization can be generally described by reactions 1-3 listed below (Kelemen and Matter, 2008).

$$2Mg_2SiO_4 + Mg_2Si_2O_6 + 4H_2O \rightarrow 2Mg_3Si_2O_5(OH)_4 \quad (1)$$

$$Mg_2SiO_4 + 2CO_2 \rightarrow 2MgCO_3 + SiO_2 \quad (2)$$

$$Mg_2SiO_4 + CaMgSi_2O_6 + 2CO_2 + 2H_2O \rightarrow 2Mg_3Si_2O_5(OH)_4 + CaCO_3 + MgCO_3 \quad (3)$$

Olivine ($Mg_2SiO_4$) and pyroxene ($Mg_2Si_2O_6$; $CaMgSi_2O_6$) react with $CO_2$-charged water to form serpentine [$Mg_3Si_2O_5(OH)_4$], magnesite ($MgCO_3$), quartz ($SiO_2$), calcite ($CaCO_3$), and aragonite ($CaCO_3$). Relatively small amounts of hydromagnesite [$Mg_5(CO_3)_4(OH)_2{\cdot}4H_2O$] (Zedef et al., 2000), brucite [($Mg(OH)_2$] (Moody, 1976), nitromagnesite [$Mg(NO_3)_2$] (Schefer and Grube, 1995), and nesquehonite ($MgCO_3{\cdot}3H_2O$) (Kastrinakis et al., 2021) may also form via reactions 4-7, respectively.

$$5Mg^{2+} + 4CO_3^{2-} + 2OH^- + 4H_2O \rightarrow Mg_5(CO_3)_4(OH)_2{\cdot}4H_2O \quad (4)$$

$$2Mg2SiO_4 + 3H_2O \rightarrow Mg_3Si_2O_5(OH)_4 + Mg(OH)_2 \quad (5)$$

$$2MgO + 4NO_2 + O_2 \rightarrow 2Mg(NO_3)_2 \quad (6)$$

$$Mg^{2+} + CO_2 + 4H_2O \rightarrow MgCO_3{\cdot}2H_2O + 2H^+ \quad (7)$$

Ongoing serpentinization of mantle peridotite bodies by meteoric waters can be identified by highly alkaline water in proximate springs, stable isotope ratios of precipitated carbonate minerals, the formation of travertines, and carbonate veins in the hosting peridotite body (Bruni et al., 2002; Cipolli et al., 2004).

Early research on ultramafic formations undergoing serpentinization led to a conceptual model for this process (Barnes and O'Neil, 1969) (Figure 1). Meteoric groundwater charged with atmospheric $CO_2$ reacts with the peridotite body near the surface and forms water that is rich in $Mg^{2+}$-$HCO_3^-$, termed Type 1 waters (Barnes and O'Neil, 1969). As this water moves underground and encounters the peridotite body, the serpentinization process is catalyzed by $CO_2$-charged $H_2O$, leading to the precipitation of $MgCO_3$ and $CaCO_3$ into veins in the peridotite. A sharp elevation in pH accompanies the mineral precipitation due to the enrichment of the water solution with $OH^-$ anions, termed Type 2 water. This Type 2 water also exhibits significant enrichment in $Ca^{2+}$ and depletion in DIC. Type 2 water is brought up to the surface where it

interacts with Type 1 water, instantly supersaturating the fluids with respect to carbonate and leading to the precipitation of calcite, aragonite, and travertine in surface springs.

A potential tool for probing carbon mineralization in these settings is carbonate clumped isotope geochemistry. The measurement of carbonate clumped isotopes in minerals precipitated from alkaline fluids can potentially constrain the mechanism(s) of kinetic isotope effects (KIEs) and rate of precipitation (Tripati et al., 2015; Watkins and Hunt, 2015; Guo, 2020; Bajnai et al., 2020). Carbonate clumped isotope analysis measures the relative abundance of multiply heavy isotope-substituted $CO_2$ isotopologues produced from acid digestion of carbonate minerals. When carbonate minerals form at thermodynamic equilibrium, they have a temperature-dependent preference of aggregation based on relative zero-point energies (Ghosh et al., 2006; Schauble et al., 2006). The relative abundance of the most common multiply-substituted mass 47 ($^{13}C^{18}O^{16}O$) and mass 48 ($^{12}C^{18}O^{18}O$) isotopologues are given by equations 8 and 9,

$$\Delta_{47} = (R47_{sample}/R47_{stochastic} - 1) \quad (8)$$

$$\Delta_{48} = (R48_{sample}/R48_{stochastic} - 1) \quad (9)$$

where $Ri$ is the ratio of the minor isotopologues ($m/z$ 47 or $m/z$ 48) relative to the most abundant isotopologue ($m/z$ 44), and $Ri_{stochastic}$ is calculated using the measured abundance of $^{13}C/^{12}C$ and $^{18}O/^{16}O$ ($R^{18}$) in the sample and the estimated abundance of $^{17}O/^{16}O$ (Eiler, 2007). The latter ratio is estimated from $R^{18}$ assuming a mass-dependent relationship between $^{18}O$ and $^{17}O$ (Daëron et al., 2016). The $\Delta_{47}$ and $\Delta_{48}$ values are given in parts per thousand (‰) (Eiler and Schauble, 2004; Ghosh et al., 2006; Eiler, 2007).

To date, most studies mechanistically exploring KIEs in carbonate minerals using clumped isotopes have focused on isotopic disequilibria in paired $\Delta_{47}$ and oxygen isotope ($\delta^{18}O$) signatures. Diffusion has been hypothesized to produce KIEs in $\Delta_{47}$-$\delta^{18}O$ in atmospheric $CO_2$ and corals (Eiler and Schauble, 2004; Thiagarajan et al., 2011). KIEs in biotic and abiotic systems associated with (de)hydration and (de)hydroxylation reactions can drive deviations from $\Delta_{47}$ equilibrium (Ghosh et al., 2006; Guo et al., 2009; Saenger et al., 2012; Falk et al., 2016; Spooner et al., 2016), as can $CO_2$ degassing, which has been used to explain $\Delta_{47}$ disequilibrium in speleothems (Hendy, 1971; Affek et al., 2008; McDermott et al., 2011; Guo and Zhou, 2019). Tang et al. (2014) hypothesized that kinetic fractionation observed in inorganic calcite precipitation experiments at pH ≥ 10 occurred due to the DIC pool not having sufficient time to achieve isotopic equilibrium prior to mineral precipitation and DIC speciation favoring $CO_3^{2-}$ at higher pH.

Previously, $\Delta_{47}$ values have been used to study $CO_2$ absorption-dominant disequilibria processes. One paper reported data from carbonate minerals in hyperalkaline springs at the Oman ophiolite and attributed disequilibria to the increase in $CO_2$ absorption in water at elevated pH (Falk et al., 2016). This study showed that carbonate minerals from these highly alkaline systems exhibit significant increases in $\Delta_{47}$, accompanied by decreases in $\delta^{18}O$ and $\delta^{13}C$. The observed pattern was found to be consistent with $CO_2$ absorption-driven disequilibrium processes related to the $CO_2$ hydroxylation reaction being expressed (Falk et al., 2016).

Recent work has shown that the “dual" carbonate clumped isotope system, the paired measurement of $\Delta_{47}$ and $\Delta_{48}$, has a characteristic relationship to equilibrium and can be used to study KIEs (Tripati et al., 2015; Fiebig et al., 2019; Guo, 2020; Bajnai et al., 2020; Lucarelli et al., 2023). The equilibrium $\Delta_{47}$-$\Delta_{48}$ dual clumped isotope relationship was constrained by theory

(Hill et al., 2014; Tripati et al., 2015; Guo, 2020; Hill et al., 2020) and more recently, by measurements from multiple studies (Fiebig et al., 2019, 2021; Bajnai et al., 2020; Lucarelli et al., 2023). However, the use of dual clumped isotope measurements for mechanistic identification of KIEs is limited. The basis relies on theoretical modeling (Hill et al., 2014; Tripati et al., 2015; Guo, 2020; Hill et al., 2020) to constrain KIEs in $\Delta_{47}$, $\Delta_{48}$, and $\delta^{18}O$ in $HCO_3^-$ and $CO_3^{2-}$ from DIC-$H_2O$ exchange driven disequilibria pathways, and (de)hydration and (de)hydroxylation reactions occurring during $CO_2$ absorption and $CO_2$ degassing. Applications to identify KIEs has been limited to a small number of measurements from biominerals including warm and cold-water coral, belemnite, and brachiopods, as well as speleothems (Bajnai et al., 2020; Lucarelli et al., 2023).

Here, we apply the novel dual carbonate clumped isotope approach, which combines the measurement of $\Delta_{47}$ and $\Delta_{48}$, to carbonate minerals from alkaline springs at The Cedars, located in a coastal mountain range formed of peridotite in Northern California. The high alkalinity, elevated pH of 11.5, and low dissolved [$CO_2$] facilitate the uptake of $CO_2$ (Lívanský, 1982; Devriendt et al., 2017), which participates in hydration or hydroxylation reactions leading to the formation of $HCO_3^-$ (reactions 10-11). These two reactions are the most important in understanding $^{18}O/^{16}O$ isotopic equilibration as they provide the only route for the direct exchange of O atoms between $H_2O$ and DIC (Zeebe and Wolf-Gladrow, 2001). Reactions 12-14 show the pathway from $HCO_3^-$ to $CO_3^{2-}$ and splitting of water molecules, and reactions 15-16 result in carbonate mineral formation. Reactions 10-16 contribute to isotopic equilibration of DIC in an aqueous solution.

$$CO_2 + H_2O \leftrightarrow H_2CO_3 \leftrightarrow HCO_3^- + H^+ \quad (10)$$

$$CO_2 + OH^- \leftrightarrow HCO_3^- \quad (11)$$

$$HCO_3^- + OH^- \leftrightarrow H_2O + CO_3^{2-} \quad (12)$$

$$HCO_3^- \leftrightarrow H^+ + CO_3^{2-} \quad (13)$$

$$H_2O \leftrightarrow H^+ + OH^- \quad (14)$$

$$Ca^{2+} + HCO_3^- \leftrightarrow CaCO_3 + H^+ \quad (15)$$

$$Ca^{2+} + CO_3^{2-} \leftrightarrow CaCO_3 \quad (16)$$

The amount of time required for clumped and oxygen isotopic equilibrium to be achieved is governed by the temperature-dependent forward and reverse rate constants for the hydration and hydroxylation reactions, as well as DIC speciation (Zeebe and Wolf-Gladrow, 2001). DIC speciation is a function of temperature and pH (Uchikawa and Zeebe, 2012; Tripati et al., 2015). At pH > 10, similar to what is observed in waters in peridotite bodies such as The Cedars, the time to reach equilibration is significantly increased due to DIC speciation being dominated by $CO_3^{2-}$, resulting in low concentrations of $CO_2$ remaining for isotopic exchange reactions 10 and 11 (Beck et al., 2005; Tripati et al., 2015; Weise and Kluge, 2020). If the DIC pool does not have

sufficient time to achieve isotopic equilibrium before precipitation begins, disequilibrium isotopic compositions may be recorded in the mineral during reactions 15-16.

In this study, our goal is to use multiple isotope systems including dual clumped isotopes ($\Delta_{47}$, $\Delta_{48}$) and bulk stable isotopes ($\delta^{18}O$, $\delta^{13}C$) to mechanistically evaluate disequilibria, examine the origin of KIEs in DIC and carbonate minerals, and study the timescales associated with mineral precipitation. Our measurements are combined with modeling to study DIC and mineral isotopic evolution. Finally, we compare our results to published work from other peridotite bodies and evaluate our approach for its potential use in geological $CO_2$ sequestration applications.

## 2. Methods

### 2.1 The Cedars Samples

The Cedars is part of the Northern California Coastal Mountain Range and is located at N38º37'14.84"/W123º08'02.13 (Figure 2). The Cedars is inside of a 700 km long surrounding body of ultramafic rocks called the Coast Range Ophiolite (CRO). The broader Coastal Mountain Range consists of peridotites in contact with part of the Franciscan Subduction Complex (FSC). The FSC consists of primarily greywacke-type sandstone, greenstone, radiolarian chert, and minor foraminiferal limestone (Blake et al., 2012). The peridotite body has an approximate surface area of 22.4 $km^2$ (3.5 km width, 6.4 km length) and extends 1-2 km below the surface (Coleman, 2000). The peridotite body consists primarily of olivine, orthopyroxene, and clinopyroxene in varying proportions as harzburgite (75% olivine and 25% orthopyroxene/clinopyroxene) and dunite (100% olivine) (Coleman, 2000). Interactions between the peridotite body and groundwaters derived from multiple sources has resulted in serpentinization of 5-20% of the ultramafic body, particularly around the perimeter that is in contact with the FSC, where the perimeter is predominantly composed of sheared serpentine (Coleman, 2000; Blake et al., 2012).

Groundwater discharge from the ultramafic body is highly alkaline, enriched in $Ca^{2+}$ and $OH^-$, and is brought to the surface through various springs in the area (Coleman, 2004; Sleep et al., 2004) where it mixes with relatively neutral pH surface waters charged with atmospheric $CO_2$ at an elevation between ~275-335 m above sea level (Barnes and O'Neil, 1969; Morrill et al., 2013).

The samples used for this study are comprised of $CaCO_3$ and were collected from The Cedars by Christensen et al. (2021), spanning eight visits in 2013, 2014, 2016, and 2018. Four major sites seen in Figure 2 were sampled: NS1 "Wedding Cake" (samples: A, Q), The Barnes Spring Complex (BSC) (samples: AA, Alpha, C1, P, PA-C2, PB-C2, PE-C2, PE-C3, S, T1, T2, T3a, T3b, T4, T5, U, V, X), Grotto Pool Springs (GPS) (samples: J, K, L), and the "New Pool" (sample: B). The "Wedding Cake" is at the NS1 location above the Mineral Falls. The $CaCO_3$ samples were collected from several different localities adjacent to the springs seen in Figure 2: (1) partially consolidated materials from rims of pools; (2) precipitates from the surface of pools, also known as floes; (3) dendritic forms and encrustations from sites of creek-spring mixing; (4) unconsolidated material, also known as snow, from the bottom of the pools; and (5) solid, old travertine deposits, taken as a hand sample representing different layers, collected from the BSC. Any consolidated, or partially consolidated surface materials were skimmed from the surface or captured on screens based on the location they were collected from. Specific sample information,

including composition and location of recovery, is listed in Table 1. The terminology used to describe samples in this paper is after Christensen et al. (2021).

Water samples from the high pH springs were taken using a 0.22 µm Millipore filter unit, acidified to a pH of 2 using $HNO_3$, and collected in high-density polyethylene (HDPE) bottles (Christensen et al., 2021). The pH of the water was measured on site using a Thermo-Scientific, Orion hand-held pH meter. Temperature measurements were taken of the water source at the time of carbonate sample recovery (Christensen et al., 2021).

## 2.2 Analysis and Instrumentation

All clumped isotopic measurements were made in the Eagle-Tripati laboratory using two Nu Instruments Perspective isotope ratio mass spectrometers (IRMS) with methods described in detail in prior publications (Upadhyay et al., 2021; Lucarelli et al., 2023). Here we will refer to the first IRMS as Nu Perspective-1, and the second as Nu Perspective-2a and Nu Perspective-2b, as measurements on the latter instrument used two configurations. Both instruments and all configurations have been shown to produce statistically indistinguishable $\Delta_{47}$ (Upadhyay et al., 2021; Lucarelli et al., 2023) and $\Delta_{48}$ values (Lucarelli et al., 2023), with standard values that agree with published values from other laboratories for $\Delta_{47}$ (Bernasconi et al., 2021) and $\Delta_{48}$ (Bajnai et al., 2020; Fiebig et al., 2021; Swart et al., 2021).

Briefly, we describe analysis and instrumentation here. For this work, measurements were made between September 2018 to November 2021. The general configuration used for clumped isotope measurements on these two instruments is (1) phosphoric acid digestion of 0.5 mg $CaCO_3$, (2) evolved $CO_2$ gas purification, and (3) isotopic measurements via the mass spectrometer.

The Nu Perspective IRMS is optimized for clumped isotope analysis with secondary electron suppression, which increases the signal-to-noise ratio. Energy filters and quadratic lenses fitted in front of the Faraday collectors for *m/z* 47, 48, and 49 drives the suppression. The detectors for *m/z* 44, 45, and 46 are registered through $3x10^8$, $3x10^{10}$, and $3x10^{11}$ Ω resistors, respectively. The detectors for *m/z* 47, 48, and 49 are registered with $3x10^{12}$ Ω resistors. A dual-inlet system allows for the input of the sample gas and a reference gas controlled by a bellows system that inputs both gasses through a changeover block, so the sample and reference gases can be compared in real-time. The reference gas and sample gas pressures are precisely matched with continuous pressure adjustments to achieve 24 V on mass 44 at the start of every acquisition block, and the pressure varies between 24-9 V during an acquisition block. Data were taken in 3 blocks of 20 cycles, for a total of 60 cycles of sample to standard comparison, with an 8-second changeover delay and 20 seconds of integration per cycle, for a total integration time of 1200 seconds.

Nu Perspective-1 and Nu Perspective-2a used an in-house built, automated system commonly referred to as the "Autoline," similar to the system from Passey et al. (2010). The autoline consists of (1) a Costech Zero Blank autosampler made of stainless steel that is capable of pulling high vacuum, (2) a common acid bath (CAB) containing 105 wt% phosphoric acid where 0.5 mg of $CaCO_3$ is reacted at 90 ºC, (3) cryogenic traps (dry ice and ethanol, and liquid nitrogen) for $CO_2$ purification through removal of water and other gases with low vapor pressures, and collection of $CO_2$, (4) an in-line elemental-silver wool (Sigma-Aldrich) column to remove sulfur compounds from the gas mixture, (5) a gas chromatograph (GC) column (UHP Helium carrier gas, Porapak Type-Q TM 50/80 mesh column packing material) held at -20 ºC during the gas transit to separate $CO_2$ from the remaining components of the produced gas

mixture, and (6) a final cryogenic purification stage before transfer of $CO_2$ into the bellows of the mass spectrometer.

Nu Perspective-2b uses a Nu Carb Sample Digestion System instead of a CAB, where 0.5 mg of $CaCO_3$ is digested at 70°C in individual glass vials with 105 wt% phosphoric acid. The sample gas is cryogenically purified in liquid nitrogen-cooled tubes called coldfingers before passing through a relatively short GC column packed with Porapak Type-QTM 50/80 and silver wool. This instrument operates under vacuum pressure and does not use a carrier gas.

#### 2.2.1 *Standardization and Data Processing*

Data was processed and corrected using Easotope 64-bit, release version 20201231 (John and Bowen, 2016) with IUPAC parameters (Brand et al., 2010; Daëron et al., 2016). The $CO_2$ reference gas used to establish real-time comparison to unknown sample compositions was sourced from Oztech and has an isotopic composition as follows: $\delta^{18}O_{VSMOW}$ = 24.9 ‰; $\delta^{13}C_{VPDB}$ = -3.56 ‰. The $\Delta_{47}$ values are reported in the Intercarb-Carbon Dioxide Equilibrium Scale (I-CDES) reference frame, meaning they were normalized to nominal carbonate standard values for ETH-1, ETH-2, and ETH-3 determined in Bernasconi et al. (2021), and additional in-house standards with values also determined in the I-CDES reference frame (Upadhyay et al., 2021; Lucarelli et al., 2023). The $\Delta_{48}$ values are reported in the Carbon Dioxide Equilibrium Scale (CDES 90) reference frame and normalized to carbonate standards values digested at 90 °C reported in Lucarelli et al. (2023). The standards used in empirical transfer functions (ETFs) for data normalization, using methods detailed in Dennis et al. (2011), include Carmel Chalk, CM Tile (Carrara Marble Tile), ETH-1, ETH-2, ETH-3, ETH-4, and Veinstrom (Upadhyay et al., 2021; Lucarelli et al., 2023). International standards ETH-1 and ETH-2 (Bernasconi et al., 2018, 2021) were used for non-linearity corrections associated with both $\Delta_{47}$ versus $\delta^{47}$ and $\Delta_{48}$ versus $\delta^{48}$ raw data. Both the ETFs and nonlinearity corrections are calculated using a moving average of ±10 standard replicates. The clumped isotope measurement errors are reported as ±1 standard error (SE) and ±1 standard deviation (SD), and the carbon and oxygen isotope measurement errors are given as ±1 SD. All data regressions were determined in PRISM Version 9.5.0 for macOS using the function "simple linear regression", where the slope and intercept error are reported as ±1 SE.

The reproducibility of standard $\Delta_{47}$ and $\Delta_{48}$ values on each instrument configuration are given in Table S1, and all sample and standard replicate data are reported in Tables S2 and S3, respectively. Figures S1-S3 show the ETH-1 and ETH-2 values from each correction interval. Figure S4 shows the standard residual values (measured value – expected value), and Table S4 reports statistical tests (D'Agostino and Pearson test, performed in PRISM) which indicate standard residuals from each instrument configuration were normally distributed. All supplemental tables and information on clumped isotope data quality assurance can be found in the Data Availability statement.

### 2.3 Modeling of DIC-$H_2O$-$CO_2$ System Using IsoDIC

To study the time evolution of the $HCO_3^-$ and $CO_3^{2-}$ endmembers in a $CO_2$ absorption-driven pathway that simulated the conditions of springs at The Cedars, we used the IsoDIC modeling software developed by Guo and Zhou (2019) and Guo (2020). This modeling software simulates reactions 10-14, predicting kinetic isotope fractionation in oxygen and clumped isotopes in a DIC-$H_2O$-$CO_2$ system from (de)hydration and (de)hydroxylation reactions. The

model tracks the isotopologue reactions involving all major isotopes of C and O, for a total of 155 reactions. The forward and reverse rate constants were estimated using equation 17,

$$k^* = a_{KIE} * k \quad (17)$$

where $k$ is the rate constant of the isotopically unsubstituted reactions, and $a_{\mathrm{KIE}}$ is the kinetic fractionation factor (KFF) for the isotopically substituted reactions. The product of these variables yields $k^*$, the modified rate constant for the isotopically substituted reactions. (De)hydration and (de)hydroxylation reactions, reactions 10-11, are the only reactions that contribute to isotopic fractionation where reactions 12-14 are assumed to be at equilibrium due to their relatively fast reaction rates when compared to reactions 10 and 11 (Guo and Zhou, 2019; Guo, 2020).

Parameters measured *in-situ* for surface floe samples (Samples L, P, U, V, PE-C2, PB-C2, and X) from The Cedars were used to simulate conditions associated with The Cedars Springs (Morrill et al., 2013). The following parameters were input into the IsoDIC software to perform modeling in the $CO_2$ absorption regime: (1) solution temperature = 17.5 ºC, (2) solution pH = 11.5, (3) air $pCO_2$ = 400 ppm, (4) $\delta^{13}C_{VPDB}$ of air = -8.431 ‰, and (5) $\delta^{18}O_{VPDB}$ of water = -36.3±0.6‰, taken as the average of measurements from the NS1, GSP1, and BSC locations (Morrill et al., 2013). The system evolution time parameter was set to 1, 10, 50, 100, and 1000 hours to simulate different timescales for the evolution of the $HCO_3^-$ and $CO_3^{2-}$ DIC species. We note that modern samples were collected from locations where surface creek (pH = 8.7) and spring waters (pH = 11.5) are mixing, resulting in a potential drop in pH to an intermediate value (pH = 8.7 to 11.5) that would reduce equilibration times from the longer values associated with highly alkaline solutions. The equations used by this model are described in the Supplementary Material S.1.

The conversion of carbonate minerals into gaseous $CO_2$ is associated with a temperature-dependent preferential removal of $^{16}O$ relative to $^{18}O$ and is corrected by an acid fractionation factor (AFF), denoted by $y$ in equations 18 and 19 (Guo et al., 2009).

$$\Delta_{47} = \Delta_{63} + y \quad (18)$$

$$\Delta_{48} = \Delta_{64} + y \quad (19)$$

An AFF is applied to measured $\Delta_{47}$ and $\Delta_{48}$ values for comparison to modeled $\Delta_{63}$ and $\Delta_{64}$ values. The reference frame and temperature to which the value is being converted also dictates the value of $y$. An AFF of $y$ = 0.196 ‰ was used in the conversion between $\Delta_{63}$ and $\Delta_{47}$ values, and an AFF of $y$ = 0.131 ‰ was used in the conversion between $\Delta_{64}$ and $\Delta_{48}$ values (Lucarelli et al., 2023).

### 2.4 Modeling of the $CaCO_3$-DIC-$H_2O$ System Using COAD

To model the KIEs in the clumped and stable isotope data of the carbonate minerals with respect to the conditions at The Cedars, we used the COAD (Carbon, Oxygen, α, Δ) model (Watkins and Devriendt, 2022), which builds upon the ExClump38 model (Chen et al., 2018; Uchikawa et al., 2021) by including the mineral precipitation reactions and growth rates (Watkins and Hunt, 2015). Mineral growth rates are important for two reasons. First, it has been hypothesized the KIEs attending these reactions can lead to differences between the clumped

isotope composition of the solid phase relative to DIC (Tripati et al., 2015). Second, the mineral growth rates affect the reversibility of the hydration and hydroxylation reactions such that fast growth rates pull these reactions closer to the kinetic limit (Watkins and Devriendt, 2022).

For comparison between outputs from COAD and IsoDIC, we used the same KFFs and model input parameters for isotopic values, temperature, and pH in our calculations (see the previous section). The COAD model involves a total of 17 differential equations to model reactions 10-16, which track the evolution of the $\delta^{18}O$, $\delta^{13}C$, $\Delta_{47}$, and $\Delta_{48}$ values of DIC species in solution and the precipitating $CaCO_3$ (Watkins and Hunt, 2015; Watkins and Devriendt, 2022). The rate constants associated with precipitation reactions 15 and 16 are mass-dependent, and the flux of precipitated $CaCO_3$ is controlled by the $[Ca^{2+}]$ and $[CO_3^{2-}]$ (Watkins and Hunt, 2015). In contrast to the IsoDIC model, this model only describes the most abundant isotopologues for the respective masses, while IsoDIC describes all isotopologues in the DIC-$H_2O$ system. The COAD model was also used to calculate the steady-state isotopic values as a function of mineral precipitation rate ($R_p$). A description of the equations and parameters used are reported in the Supplementary Material S.2. The code used is available for download in the Data Availability Statement.

### 2.5 Estimation of $CO_2$ Sequestered at The Cedars

Due to the similarity in rock composition and water pH in the Samail Oman and The Cedars peridotite and associated springs (Kelemen and Matter, 2008; Morrill et al., 2013; Christensen et al., 2021), we estimated the rate and amount of $CO_2$ that could naturally be sequestered at The Cedars based on an approach used in previous work from Kelemen and Matter (2008) for a peridotite body in Oman. Kelemen and Matter (2008) estimated that in the Omani ophiolite, the travertines and carbonate veins comprised a volume of roughly $5.5 \times 10^7$ $m^3$, or a minimum of $\approx 10^{11}$ kg of $CO_2$. In addition, for the determination of rates of carbonation for the two different types of waters (Figure 1), they make two key assumptions. First, in Type 1 waters, they assume the complete consumption of DIC to precipitate carbonate minerals as Type 2 waters are formed. Second, they assume that differences in dissolved $Ca^{2+}$ between the two types of waters leads to calcite precipitation as Type 2 waters reach the surface. Using this approach, they calculate that carbonate mineralization in the region consumes ~$4 \times 10^7$ kg of atmospheric $CO_2$ per year, or $\approx$2 tons/$km^3$/year of peridotite.

We also estimated the total sequestration potential at The Cedars. For this calculation, we summed the amount of $CO_2$ that would be consumed if the total amount of Mg, Ca, and Fe in relict olivine was consumed by carbonation. We assumed that The Cedars peridotite is composed of 70 % olivine which is 43.82 weight% Mg, 5.34 weight% Fe, and 0.52 weight% Ca (Coleman, 2000; Blake et al., 2012; Morrill et al., 2013), has a volume of 44.8 $km^3$ (Coleman, 2000), a density of partially serpentinized peridotite of 2800 km/$m^3$ (Carnevale, 2013), total mass of $1.25 \times 10^{14}$ kg (calculated from the volume and density), and a carbonation rate of 1 % (Kelemen and Matter, 2008). Below, we show how this calculation was performed for Mg.

$$(1.25 \times 10^{14}\ \text{kg}) \times 0.70 \times 0.4382 \times 0.01 \times \frac{CO_2\ 44\ \text{g/mol}}{\text{Mg}\ 24.3\ \text{g/mol}} = 7.0 \times 10^{11}\ \text{kg}\ CO_2\ \text{sequestered}$$

We used the conservative estimate of calcite growth rate in The Cedars springs of $4.8 \times 10^7$ mol/$m^2$/s (Christensen et al., 2021) to estimate the rate of $CO_2$ sequestered in the springs per year.

For comparison, we report a set of calculations for the CRO from Carnevale (2013) that also utilize the methods of Kelemen and Matter (2008). To estimate the amount of $CO_2$ sequestered in the CRO per year, we used the $CO_2$ sequestration potential reported in Carnavale (2013) and the natural carbonation rate for peridotite determined in Kelemen and Matter (2008).

Additionally, Kelemen and Matter (2008) assumed the natural rates of $CO_2$ uptake could be enhanced by ~$10^6$ times by drilling and hydraulic fracturing of the rock to increase the reactive surface area, initial heating of the rock to 185 ºC using hot fluids, followed by the injection of $CO_2$ (pressure = 300 bars, temperature = 25 ºC, flow rate = 0.040 m/s). They estimate this would result in a sequestration rate of ~$2 \times 10^9$ tons of $CO_2$ sequestered per $km^3$. This rate was used to estimate the time elapsed before all peridotite would be converted into carbonate minerals from enhanced *in situ* carbonation at The Cedars, CRO, and Oman ophiolite. The parameters used in all calculations are reported in Table S5.

## 3. Results

### 3.1 Dual Clumped Isotope Analysis

Dual clumped isotope values ($\Delta_{47}$, $\Delta_{48}$) are reported for samples from The Cedars in Figure 3 and Table 2. The $\Delta_{47}$ and $\Delta_{48}$ values range from 0.595‰ to 0.791‰ and -0.506‰ to 0.282‰, respectively. The samples that are within error (±1 SE) of an equilibrium regression (Lucarelli et al., 2023) are A, AA, B, and J. All other samples exhibit apparent KIEs, with the greatest departure from equilibrium in sample V ($\Delta_{47}$ = 0.779‰; $\Delta_{48}$ = -0.506‰; Figure 3). The sampling location of each sample can be seen in Figure 2. A linear regression of the $\Delta_{48}$-$\Delta_{47}$ values from The Cedars yields a slope of -3.223±0.519.

### 3.2 Clumped and Stable Isotopes

The $\delta^{18}O$ and $\delta^{13}C$ values for The Cedars samples range from -19.3‰ to -0.1‰ and -27.3‰ to -9.2‰, respectively (Table 2). The $\Delta_{47}$ of modern and Holocene samples from The Cedars are plotted versus $\delta^{18}O$ and $\delta^{13}C$ and compared to samples from alkaline springs in the Oman ophiolite (Falk et al., 2016) (Figure 4A, C). The measured values from The Cedars and Oman are also compared to calculated equilibrium values. The calculated equilibrium $\delta^{18}O_{CaCO3}$ range was determined to be -8.2‰ to -6.6‰ for calcite and aragonite (Kim and O'Neil, 1997; Kim et al., 2007; Dietzel et al., 2009), given The Cedars $\delta^{18}O_{water}$ value of -36.3±0.6‰, taken as the average of measurements from the NS1, GSP1, and BSC locations (Morrill et al., 2013). The equilibrium $\Delta_{47}$ value (Lucarelli et al., 2023) for the average water temperature of 17.5±1 ºC (Christensen et al., 2021; Morrill et al., 2013) was determined to be 0.616±0.003‰. All samples show departures from equilibrium oxygen isotope values.

Linear regressions through The Cedars and Oman datasets are in strong agreement. The $\Delta_{47}/\delta^{18}O$ and $\Delta_{47}/\delta^{13}C$ data regressions for The Cedars samples both exhibit slopes of -0.009±0.001 (Figure 4A, C). The $\Delta_{47}/\delta^{18}O$ and $\Delta_{47}/\delta^{13}C$ data regressions for the Oman samples (Falk et al., 2016) exhibit slopes of -0.006±0.002 and -0.005±0.002, respectively. When The Cedars and Oman datasets are combined, the slopes of the $\Delta_{47}/\delta^{18}O$ and $\Delta_{47}/\delta^{13}C$ data regressions are -0.007±0.001 and -0.006±0.001, respectively.

The $\Delta_{48}$ versus $\delta^{18}O$ and $\delta^{13}C$ values for The Cedars are also reported (Figure 4B, D; Table 2), and compared to equilibrium. The equilibrium $\Delta_{48}$ value (Lucarelli et al., 2023) for the

455 average water temperature of 17.5±1 ºC (Morrill et al., 2013; Christensen et al., 2021) was
456 determined to be 0.255±0.002‰. The $\Delta_{48}/\delta^{18}O$ and $\Delta_{48}/\delta^{13}C$ regression slopes are 0.041±0.003
457 and 0.038±0.005, respectively.
458
459 **3.3 Clumped and Oxygen Isotope Disequilibrium**
460 The extent of clumped and oxygen isotope disequilibrium ($\Delta\Delta_{47}$, $\Delta\Delta_{48}$, and $\Delta\delta^{18}O$) in The
461 Cedars was calculated by taking the difference between the measured values and calculated
462 equilibrium values (Kim and O'Neil, 1997; Kim et al., 2007; Dietzel et al., 2009; Lucarelli et al.,
463 2023) (Table 2). The $\Delta\Delta_{47}$, $\Delta\Delta_{48}$, and $\Delta\delta^{18}O$ values are compared to theoretical slopes
464 determined by Guo (2020) for various kinetic processes (Figure 5). The $\Delta\delta^{18}O$ values range from
465 -12.7‰ to 7.2‰, while $\Delta\Delta_{47}$ and $\Delta\Delta_{48}$ values range from -0.021‰ to 0.175‰ and -0.761‰ to
466 0.027‰, respectively (Table 2). The slopes of the $\Delta\Delta_{47}/\Delta\delta^{18}O$, $\Delta\Delta_{48}/\Delta\delta^{18}O$, and $\Delta\Delta_{48}/\Delta\Delta_{47}$ are -
467 0.009±0.001, 0.040±0.003, and -3.223±0.519, respectively.
468
469 **3.4 Modeled Clumped Isotope Evolution**
470 Measured $\Delta_{47}$ and $\Delta_{48}$ values for The Cedars samples were compared to IsoDIC (Guo, 2020)
471 model predictions for the time-dependent isotopic evolution of $HCO_3^-$ and $CO_3^{2-}$ (Figure 6A).
472 The measured values are consistent with the range of $\Delta_{47}$ and $\Delta_{48}$ values predicted by the model
473 for $HCO_3^-$ and $CO_3^{2-}$. The measured $\Delta_{47}$ and $\Delta_{48}$ values were also compared to model predictions
474 for $CaCO_3$, $HCO_3^-$, $CO_3^{2-}$, and equilibrated inorganic carbon (EIC) using the COAD model
475 (Watkins and Devriendt, 2022) (Figure 6B-D). Measured $\delta^{18}O$ and $\Delta_{47}$ values are largely
476 consistent with model predicted values, however, the $\Delta_{48}$ values for the ancient travertine
477 samples and snow samples collected from the bottom of the pool (Table 1) were offset from the
478 COAD model predicted values for $CaCO_3$ by up to 0.1 ‰ (Figure 6D).
479 The average $\Delta_{47}$ and $\Delta_{48}$ values and growth rate for samples with relatively large KIEs that
480 were collected at the BSC springs location (samples U, V, X; Figure 2) were compared to COAD
481 model predictions for the evolution of clumped isotope values of calcite from varying
482 precipitation rate (Figure 6E-F). The model accurately predicted the measured $\Delta_{47}$ value of
483 0.744±0.010‰ within 1 SE, while the measured $\Delta_{48}$ value of -0.407±0.037‰ was offset from the
484 model predicted value of -0.264‰ by -0.143‰.
485
486 **3.5 $CO_2$ Sequestration**
487 We estimate the peridotite body at The Cedars could sequester a maximum of ~$7.39 \times 10^8$
488 tons of $CO_2$ at a natural rate of ~63 tons/year. It would take ~$1 \times 10^7$ years to reach the
489 maximum amount of sequestration (Figure 7). The Cedars springs could sequester an additional
490 ~4 tons/year. If we utilize estimates of the volume and total sequestration potential of the CRO
491 (Carnevale, 2013), we estimate that ~$1.2 \times 10^4$ tons of $CO_2$ could be naturally sequestered per
492 year at the CRO, with the maximum $CO_2$ sequestration potential achieved after ~$8.3 \times 10^6$ years.
493 If the enhanced *in situ* carbonation rate of ~$2 \times 10^9$ tons $CO_2/km^3$/year described in Kelemen and
494 Matter (2008) were used, all olivine in the CRO could be converted into carbonate minerals in
495 less than 50 years.
496
497 **4. Discussion**
498
499 **4.1 Broad Patterns in Multi-Isotope Space: Comparison of Sample Sets**

The similarity in $\Delta_{47}/\delta^{18}O$ and $\Delta_{47}/\delta^{13}C$ regression slopes for The Cedars data and data from surface springs and veins in the Samail ophiolite of Oman (Falk et al., 2016) (Figure 4A, C) suggest the same processes are driving disequilibrium in both systems. However, regional, and possible local and temporal, variations in the $\delta^{18}O$ of waters, and $\delta^{13}C$ of DIC, also are reflected in these data. For example, the Oman dataset (Falk et al., 2016) may have larger fluctuations in $\delta^{13}C$ and $\delta^{18}O$ due to the amount and type of samples analyzed, and greater fluctuations in DIC $\delta^{13}C$ and meteoric water $\delta^{18}O$ due to the significantly larger area, 200 km x 50 km, of the Oman site (Christensen et al., 2021). In contrast, the $\Delta_{47}$-$\Delta_{48}$ dual clumped isotope approach allows for mechanistic fingerprinting of the processes associated with disequilibria, and a rough estimation of timescales for equilibration. This represents a major advancement in the clumped isotope field as data from different localities, natural and synthetic, can be directly compared for potential sources of disequilibrium. An additional benefit of clumped isotopes is the method can be used without knowledge of additional parameters such as the isotopic composition of the parent fluid or DIC source.

The majority of Cedars samples exhibit an enrichment in $\Delta_{47}$ accompanied by a depletion in $\Delta_{48}$, with a $\Delta\Delta_{48}/\Delta\Delta_{47}$ slope of -3.223±0.519. Our observed slope is intermediate between the theoretically calculated slopes for KIEs from $CO_2$ hydration and hydroxylation reactions during $CO_2$ absorption (25 ºC; pH 9) and in high pH travertine (28 ºC; pH 11.5), which have slopes of -1.72 and -8.33, respectively (Guo, 2020) (Figure 5). Thus, the disequilibria at The Cedars and Oman are occurring through a similar pathway that is largely associated with $CO_2$ hydroxylation. We note a similar trend was also reported by Bajnai et al. (2020) in their dual-clumped investigation of cold-water coral, warm-water coral, and brachiopods, and in a cold-water coral sample reported by Lucarelli et al. (2023). Both studies concluded hydration/hydroxylation during $CO_2$ absorption drove kinetic biases in the dual clumped isotope values.

### 4.2 (Dis)Equilibrium Within The Cedars Depends on Sample Location

Sample location within The Cedars was a major factor influencing whether bulk and clumped isotopic data exhibited departures from equilibria, likely linked to variations in DIC sources (i.e., Type 1 and Type 2 waters) and equilibration time. Modern samples L, P, U, V, PB-C2, and PE-C2 collected from surface pool floes located at the BSC and GPS locations (Figure 2) exhibited the greatest KIEs (Figures 3-6). At these two localities, KIEs could be related to the rapid uptake of $CO_2$ at the surface, leading to similarly rapid carbonate mineral precipitation at the air and water interface. These results would be consistent with the interpretations of bulk stable isotopic data by Christensen et al. (2021), who investigated the dynamics associated with $CaCO_3$ precipitation and stable isotope fractionation in surface floes, and argued that at The Cedars, KIEs may be the largest when $CaCO_3$ precipitates at the surface of the springs. The BSC location had a high saturation state ($\Omega$) value of ~13, while the GPS location had an $\Omega$ value of ~5. The $[CO_2]$ at the surface layer at the BSC location was calculated to be $1.6 \times 10^{-5}$ mol/kg-solution, several orders of magnitude higher than the concentration of the bulk pool. The rate of $Ca^{2+}$ replenishment from the springs at the BSC was determined to be $1.5 \times 10^{-6}$ mol/s, which is comparable to the DIC flux from the atmosphere. The $CO_2$ from the atmosphere is converted to $HCO_3^-$ via hydroxylation (reaction 11), with rapid and near-quantitative conversion to $CO_3^{2-}$ (Tripati et al., 2015). With this higher influx of $CO_2$ and precipitation of $CaCO_3$, the surface pH is reduced slightly from 11.5 in the bulk pool springs to 11.0 at the surface (Christensen et al., 2021). However, the pH is still high enough to favor $CO_3^{2-}$ DIC speciation (Uchikawa and Zeebe, 2012; Tripati et al., 2015) preventing isotopic equilibrium through exchange reactions

associated with the other DIC species. In addition, because the concentration of DIC is so high at the surface due to the large $CO_2$ gradient between the water and atmosphere, the supersaturation state of $CaCO_3$ is also considerably high, further promoting rapid precipitation of $CaCO_3$ outside of isotopic equilibrium (Christensen et al., 2021).

The modern "snow" samples C1, K, PA-C2, PE-C3 and PB-C1 exhibited KIEs that were intermediate between equilibrium and pool floe samples (Figure 3). The term snow is used to describe the physical appearance of fine particulates of $CaCO_3$ aggregating at the bottom of the pools, however, their texture is similar to surface floe samples (Christensen et al., 2021). The thin-film model (Christensen et al., 2021) for surface dynamics suggests that as the surface floes thicken or are perturbed by falling debris, $CaCO_3$ aggregates detach and sink deeper into the springs. The floes would carry some surface waters with the particles (Christensen et al., 2021), and thus could mix in a pool of DIC that is not in isotopic equilibrium, driving KIEs in the clumped and bulk isotope signatures. Even though these detached layers, composed of a mixture of particle aggregates and solution, have moved away from the surface where the majority of rapid precipitation is occurring, isotopic equilibration of DIC within the detached layer is still hindered by the high pH of 11.5 (Beck et al., 2005), which favors hydroxylation and $CO_3^{2-}$ as the most abundant DIC species (Tripati et al., 2015). Given water temperatures, DIC in this fragmented layer can retain its kinetic signature for tens of days at a pH of 11.5 (Usdowski et al., 1991; Beck et al., 2005) which can contribute to the KIEs in dual clumped and bulk isotopes. DIC mixing can also drive deviations from equilibrium in $\Delta_{47}$ values (Defliese and Lohmann, 2015).

Modern samples A, AA, B, and J fell within 1 SE of clumped isotope equilibrium (Figure 3). They were collected where fresh creek water mixed with spring water at the New Pool and BSC localities, where the pH and the influx of $Ca^{2+}$ are reduced, leading to potentially more favorable conditions for isotopic equilibration in the DIC-$H_2O$-$CO_2$ system. These samples reflect the composition of isotopically equilibrated DIC from the creek or surface water (pH 7.8-8.7) that occasionally mixes with the high-pH springs (Christensen et al., 2021). The $\Delta_{47}$-reconstructed temperature for the near equilibrium samples is 13.9±3.8 ºC and 14.2±3.5 ºC, using calibrations from Lucarelli et al. (2023) and Andersen et al. (2021), respectively. These reconstructed temperatures are within error (1 SD) of the average yearly temperature at The Cedars of 17.5±1 ºC (Morrill et al., 2013; Christensen et al., 2021).

Ancient travertine samples collected from rim formations at the NS1 locality (Alpha, T1, T2, T3a, T3b, T4, and T5) display a range of disequilibrium values (Figures 3-6). This range could be due to post-depositional events such as recrystallization in the presence of surface and groundwater mixing, which could have shifted disequilibrium isotopic values towards equilibrium in samples T1, T4, and T5. This would be analogous to what Falk et al. (2016) hypothesized occurred in Oman, where the absence of aragonite in travertine samples may have indicated post-depositional events had taken place, thereby influencing isotopic values.

### 4.3 Overall Conditions at The Cedars Result in Isotopic Disequilibrium

Several factors control the expression of KIEs in carbonate minerals from The Cedars. These include the hydroxylation favored pathway, DIC speciation, increased rate of $CO_2$ uptake into the system, and mineral precipitation prior to isotopic equilibria. Because Type 1 and 2 waters are readily mixing at the surface, a hyperalkaline environment (pH > 11) is created due to excess $OH^-$ anions present in Type 2 fluids. At a pH > 10, the hydroxylation pathway represents >95% of reactions transforming $CO_2$ to $HCO_3^-$ (McConnaughey, 1989). This high pH also

creates an environment that facilitates rapid uptake of $CO_2$ into the aqueous media (Lerman and Stumm, 1989) due to the concentration gradient created by the DIC speciation preference of $CO_3^{2-}$ at pH > 10 (Hill et al., 2014; Tripati et al., 2015). This condition, coupled with the rapid precipitation of $CaCO_3$ due to the high saturation state (Christensen et al., 2021), creates an even stronger gradient, further increasing the uptake of $CO_2$ from the atmosphere. The forward reaction rate associated with $CO_2$ hydroxylation is >1000 times the reverse reaction (Christensen et al., 2021), creating a pathway that is approximately unidirectional. We hypothesize this is preventing backwards conversion which is essential for O isotope exchange that would facilitate $\delta^{18}O$, $\Delta_{47}$, and $\Delta_{48}$ equilibrium. The high pH results in a much greater equilibration time (>40 days) being required for the DIC pool to achieve clumped and oxygen isotopic equilibria prior to mineral precipitation (Beck et al., 2005; Tripati et al., 2015; Guo, 2020; Uchikawa et al., 2021). As the system moves into the deeper parts of the spring pool (below 100 µm), there are additional fluxes including advection and diffusion of Type 2 waters, $CaCO_3$ precipitation, and EIC contribution from the surface.

### 4.4 Examination of Kinetic Isotope Effects Using Modeling

IsoDIC (Guo, 2020) modeling of disequilibria in the DIC pool used input parameters taken from the surface floe conditions of The Cedars and accurately predicted the measured range of $\Delta_{47}$ and $\Delta_{48}$ values (Figure 6A). The model was used to predict the evolution of disequilibria associated with $HCO_3^-$ and $CO_3^{2-}$ with respect to residence time in the system. The model indicated a rapid departure away from equilibria with maximum disequilibria achieved at ~1 hour of DIC residence time. This initial departure rebounds back to equilibrium as the system has more time equilibrate, where equilibrium is eventually achieved after ~1000 hours. Due to the low [$CO_2$] from DIC speciation favoring $CO_3^{2-}$ at high pH (Beck et al., 2005; Tripati et al., 2015), the migration back to equilibria at these conditions is very slow. The IsoDIC (Guo, 2020) model can be used to predict the approximate timeframe associated with precipitation at the surface, which we hypothesize to be ≤1 hour from when $CO_2$ is introduced into the surface spring system (Figure 6A). A caveat is that this model only considers the KIEs associated with the DIC pool and does not factor those associated with mineral precipitation.

Since the IsoDIC model did not consider KIEs associated with mineral precipitation, isotopic evolution was also predicted with the COAD model, which does predict KIEs from precipitation, using the same input parameters as for the IsoDIC model. This model predicted a similar trend for $\Delta_{47}$ and $\Delta_{48}$ (Figure 6B) when compared to the IsoDIC model, in terms of migration from equilibrium to disequilibrium. However, while the models starting values for $CO_3^{2-}$ and $HCO_3^-$ are very similar, as modeled precipitation starts in the COAD model, the associated KIEs from precipitation result in a maximum difference of ~0.10‰ between the simulated $CO_3^{2-}$ and $HCO_3^-$ values from the two models. Additionally, the measured $\Delta_{47}$ values and COAD predictions are in good agreement (Figure 6C), while some measured $\Delta_{48}$ values for travertine samples and snow samples collected from the bottom of the pool (Table 1) deviate from model predicted $\Delta_{48}$ values by up to 0.1 ‰ (Figure 6D). The ancient travertine samples (T1, T2, T3a, T3b, T4, T5) contained multiple layers, and therefore mixing may impact clumped isotopes (Eiler and Schauble, 2004; Defliese and Lohmann, 2015), and there is no current knowledge of possible differences in travertine versus typical calcite $\Delta_{48}$ values. Mixing may also bias clumped isotope values in the snow samples, which may experience temporal variations in DIC isotopic composition. Further, some of the snow samples have mixed minerology (aragonite, calcite, brucite), such as samples PB-C1, PE-C2, and PE-C2 (Table 1). The brucite

[$Mg(OH)_2$] composition ranges from 4-7 %, which has unknown effects on acid digestion and potentially the clumped isotope values.

COAD modeling enables us to determine and predict the rates of mineral precipitation associated with the respective system, which is constrained by measured dual clumped isotope values. The COAD model was also used to predict the dependence of $\Delta_{47}$ and $\Delta_{48}$ values from The Cedars samples on the precipitation rate (Figure 6E-F). The model accurately predicted the average $\Delta_{47}$ value at the BSC springs, given the measured precipitation rate (Christensen et al., 2021). Comparison of dual clumped data to model results supports a natural rate of carbonate precipitation of ~$4.8 \times 10^{-7}$ mol/m$^2$/s (Figure 6E). However, the model underpredicted the average $\Delta_{48}$ value (Figure 6F). This may be due to greater measurement uncertainty for $\Delta_{48}$, which is an order of magnitude greater than for $\Delta_{47}$ (1 SE for $\Delta_{47} \approx 0.001$; 1 SE for $\Delta_{48} \approx 0.01$), and no previous experimental constraints on how $\Delta_{48}$ values change from increased precipitation rates.

We find the two models provide a slightly different set of tools. The IsoDIC model focuses on the time evolution of the isotopic composition of DIC species from an initially perturbed or out-of-equilibrium state. In this framework, the steady state of the system is equivalent to the equilibrium state. By contrast, the COAD box model involves fluxes of $CO_2$ and $CaCO_3$ such that the isotopic composition of DIC species is continually perturbed. In this framework, the steady state of the system is not equivalent to the equilibrium state unless the $CO_2$ flux is extremely small compared to the size of the DIC pool. Using the COAD model, accurately measured $\Delta_{47}$ values (and possibly $\Delta_{48}$ values) can be compared to model predicted values as a function of the $CO_2$ influx and $CaCO_3$ outflux (i.e., mineral precipitation rate).

Field measurements and modeling may be useful for application to other peridotite bodies to help determine the natural mineral precipitation rates and DIC residence time. Our work here shows this approach is useful for predicting the natural rates of $CO_2$ uptake. If the rate of $CO_2$ uptake was enhanced using a feed of high-pressure $CO_2$ and hydraulic fracturing, dual clumped isotope measurements could be interpreted within a modeling framework to evaluate the enhanced rates of DIC equilibration and mineral formation.

### 4.5 Potential $CO_2$ Sequestration Application

Assuming the natural carbonation rate of peridotite consumes ~2 tons of $CO_2$/km$^3$/year (Kelemen and Matter, 2008), then the peridotite at The Cedars, surrounding ophiolite in the Coast Range, and ophiolite in Oman consume ~90, ~$1.1 \times 10^4$, and ~$4.2 \times 10^4$ tons of $CO_2$ per year, respectively (Figure 7). At the natural rate, the peridotite at The Cedars would take >$10^6$ years to achieve the maximum $CO_2$ sequestration potential of ~$7.4 \times 10^8$ tons. The peridotite at the CRO and Oman would take >$10^6$ and >$10^9$ years to reach their $CO_2$ sequestrations potentials of ~$9.7 \times 10^{10}$ (Carnavale, 2013) and ~$7.7 \times 10^{13}$ (Kelemen and Matter, 2008) tons, respectively. While these ultramafic formations provide an important natural $CO_2$ sink, the total yearly sequestration represents <<1% of current global $CO_2$ emissions of $34.9 \times 10^9$ tons (Liu et al., 2022).

Previous work by Kelemen and Matter (2008) proposed a method for enhanced *in situ* carbonation of peridotite for the Samail Ophiolite in Oman. This method greatly enhances the natural carbonation reaction (reaction 10) rate by up to $1 \times 10^6$ times by drilling and hydraulic fracturing of the rock to increase the reactive surface area, initial heating of the rock to 185 $^o$C using hot fluids, followed by the injection of $CO_2$ (pressure = 300 bars, temperature = 25 $^o$C, flow rate = 0.040 m/s) (Kelemen and Matter, 2008). After the initial heating, the exothermic

carbonation reaction maintains the system temperature at 185 ºC (Kelemen and Matter, 2008). As the reactive surface becomes depleted, the rock may require additional fracturing, although some cracking may occur from the temperature changes and increases in solid volume from mineral hydration and carbonation (Kelemen and Matter, 2008). If we assume the fully catalyzed reaction rate of ~$2 \times 10^9$ tons of $CO_2$ sequestered per year, it would take <50 years and <40,000 years, respectively, for all Mg, Ca, and Fe in the CRO and Oman peridotite to be converted into carbonate minerals (Figure 7). This would consume an enormous amount of $CO_2$, totaling >4 billion tons of $CO_2$ sequestered per year.

A hurdle to employing mineral carbonation technology in peridotite formations is that ~1 million drill holes (Kelemen et al., 2011) may be required to offset $34.9 \times 10^9$ tons (Liu et al., 2022) of anthropogenic $CO_2$ emissions per year. Further, these operations could result in deforestation (Drohan and Brittingham, 2012), loss of animal habitats (Kiviat, 2013), and contaminated wells (Holzman, 2011), as has been observed with fracking. However, it is notable that the in-situ $CO_2$ sequestration potential in peridotite bodies is high when compared to other potential technologies. High-temperature mineral carbonation reactors, which would use mineral feedstock from mines and direct $CO_2$ injection, could rapidly convert serpentine and olivine to magnesite and quartz, resulting in ~$8.8 \times 10^5$ to ~$8.8 \times 10^6$ tons of $CO_2$ sequestered per year (Power et al., 2013). The injection of $CO_2$ into ponds containing serpentinite mine tailings could sequester up to ~$1 \times 10^6$ tons of $CO_2$ per year (Power et al., 2013). This may be enhanced if the ponds utilize photoautotrophic microbes, such as algae and cyanobacteria, which use $CO_2$ as an energy source (Power et al., 2011). It is likely that multiple strategies will need to be used in parallel to reach global carbon dioxide reduction goals, which are 10 Gt/yr by 2050 and 20 Gt/yr by 2100 (UNEP, 2019).

## 5. Conclusions

We analyzed carbonate mineral samples collected from springs at The Cedars, a peridotite body in Northern California, for dual clumped and bulk stable isotopes. We combined measured $\Delta_{47}$, $\Delta_{48}$, $\delta^{18}O$, and $\delta^{13}C$ and model calculations to study kinetic isotope effects associated with $CO_2$ absorption, high pH, and precipitation rate. Our work suggests kinetic biases in dual clumped and bulk isotope values arise due to carbonate mineral precipitation from highly alkaline waters through a $CO_2$ absorption-driven pathway. Our analysis indicates that the largest KIEs are from samples recovered from surface floes. In surface floes, there is sufficient contact between the spring waters and the atmosphere where $CO_2$ absorption and rapid precipitation conditions are favored. Modern samples with isotopic values within error of equilibrium occur in locations where there is significant mixing of surface and spring waters. Other samples with kinetically biased isotopic values include "snow" samples recovered from the bottom of springs and ancient travertine samples. We report slopes ($\Delta_{48}/\Delta_{47}$, $\Delta_{47}/\delta^{18}O$, $\Delta_{48}/\delta^{18}O$, $\Delta_{47}/\delta^{13}C$, $\Delta_{48}/\delta^{13}C$) for $CO_2$ (de)hydration and (de)hydroxylation disequilibria processes from The Cedars samples. The slopes are consistent with $\Delta_{47}/\delta^{18}O$ and $\Delta_{47}/\delta^{13}C$ slopes from a peridotite body in Oman, as well as modeling predictions for KIEs from $CO_2$ (de)hydration and (de)hydroxylation.

This work sets up the potential use of the $\Delta_{47}$-$\Delta_{48}$ dual clumped isotope method, combined with modeling, to examine sites of interest for geological $CO_2$ sequestration, including in the Coast Ranges and other peridotite bodies. This relatively non-invasive method can be used to determine the natural rate of $CO_2$ uptake, mineral precipitation rate, and for determining evolution time and (dis)equilibria in DIC. We recommend expansion of dual clumped isotope

research into carbonate minerals precipitating from peridotite veins to compare surface and subsurface processes, and better understand the feasibility of sites for $CO_2$ sequestration.

## Declaration of Competing Interests

The authors declare that they have no known competing financial interests or personal relationships that could have appeared to influence the work reported in this paper.

## Acknowledgments

We thank the reviewers and editor for their helpful suggestions and thoughtful handling of the manuscript. We thank lab members past and present for their work running standards, efforts in data entry, and contributions to discussions. We thank Jade Knighton and Adiba Hassan for their support. This work was funded by the United States Department of Energy, Office of Basic Energy Sciences (DOE BES) grant DE-FG02-83613ER16402, Heising-Simons Foundation grant 2022-3314, NSF grant ICER- 2039462 for Veterans in STEM, and a Royal Society Wolfson Visiting Fellowship to Aradhna Tripati. Zeeshan Parvez, Jamie Lucarelli, Irvin Matamoros, Joshua Rubi, Kevin Miguel, Randy Flores, and Robert Ulrich acknowledge support from the above grants and from fellowships by The Center for Diverse Leadership in Science which is supported by the Packard Foundation, Sloan Foundation, Silicon Valley Community Foundation, and NSF. Zeeshan Parvez received support as a Tillman Scholar. Jamie Lucarelli received support from Cota Robles and Dissertation Year Fellowships from the University of California, Los Angeles. We thank Ben Elliot and members of the Eagle-Tripati laboratory for their technical support in mass spectrometry. Support to John Christensen was provided by the United States Department of Energy, Office of Basic Energy Sciences (DOE BES) under Award # DE-AC02-05CHii231 to Lawrence Berkeley National Laboratory. AT initiated and supported the work. AT and JC designed the research. ZP and JL wrote the manuscript with guidance from AT and RE and input from all coauthors. JC provided samples. JL, ZP, IM, JR, KM, BE, RF performed the isotope analyses and calculations with input from AT. ZP performed the IsoDIC and COAD model calculations. JL performed the $CO_2$ sequestration calculations. JW modified the COAD model for this project and provided training for implementation and post-processing. ZP, JL, RU, RE contributed insights to data analyses and interpretations. AT and RE advised ZP, IM, JR, KM, RF, JL, and RU.

## Data Availability

Replicate data for samples and standards, statistical analyses of standards, parameters used in $CO_2$ sequestration calculations, information about clumped isotope data quality assurance, and model codes are available through Zenodo at https://doi.org/10.5281/zenodo.7982809 .

## Figures

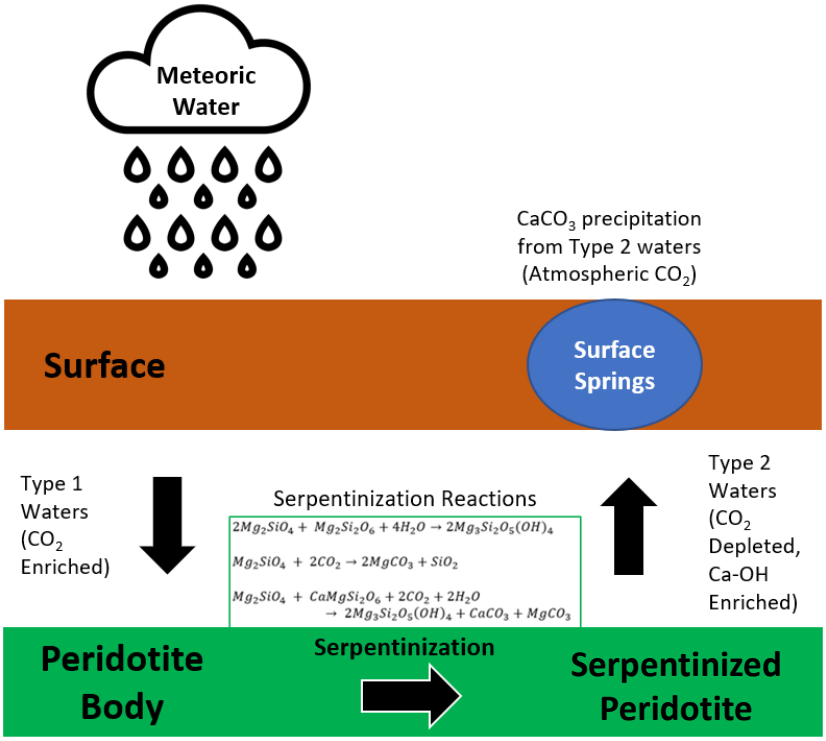


**Figure 1.** Processes associated with $CO_2$ absorption and transformation at The Cedars. Surface waters from meteoric sources are enriched with $CO_2$ from the atmosphere ("Type 1" waters) and then seep into the ground and interact with ultramafic peridotite. Through a series of serpentinization reactions (reactions 1-3), various carbonate minerals precipitate and are sequestered in pores and fractures resulting in veins in the peridotite body. Reaction by-products are ejected into pore waters, creating waters which are enriched in $Ca^{2+}$ and $OH^-$ ions, and depleted in $CO_2$ ("Type 2" waters), which are then shuttled to the surface. Type 1 and Type 2 waters interact at the surface in the presence of atmospheric $CO_2$, resulting in rapid precipitation of $CaCO_3$. Terminology from Barnes and O'Neil (1969).

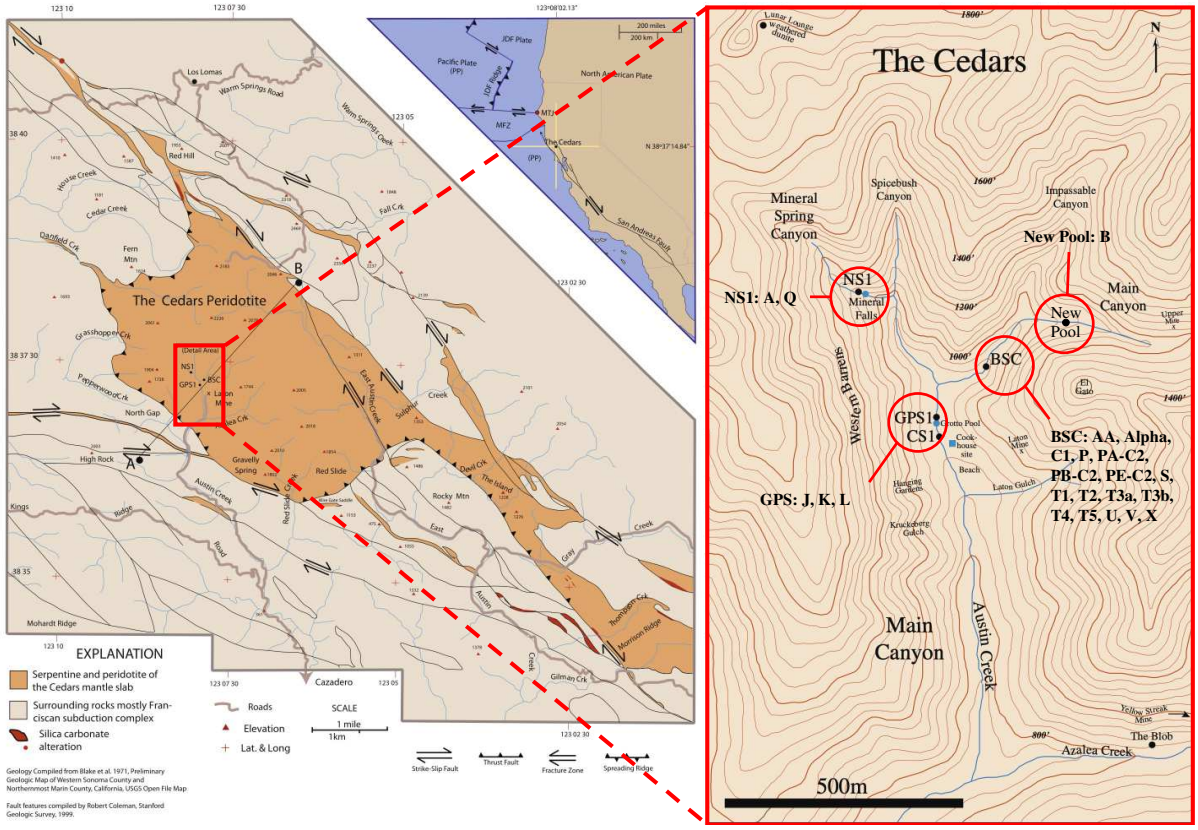


**Figure 2.** Map of The Cedars site showing the location of samples. Sample locations indicated in the right panel include NS1 (samples: A, Q,), Grotto Pool Springs (GPS) (samples: J, K, L), Barnes Spring Complex (BSC) (samples: AA, Alpha, C1, P, PA-C2, PB-C2, PE-C2, PE-C3, S, T1, T2, T3a, T3b, T4, T5, U, V, X), and New Pool (sample: B). The "Wedding Cake" is located at the NS1 location above the Mineral Falls. Modified from Morrill et al. (2013) and Christensen et al. (2021).

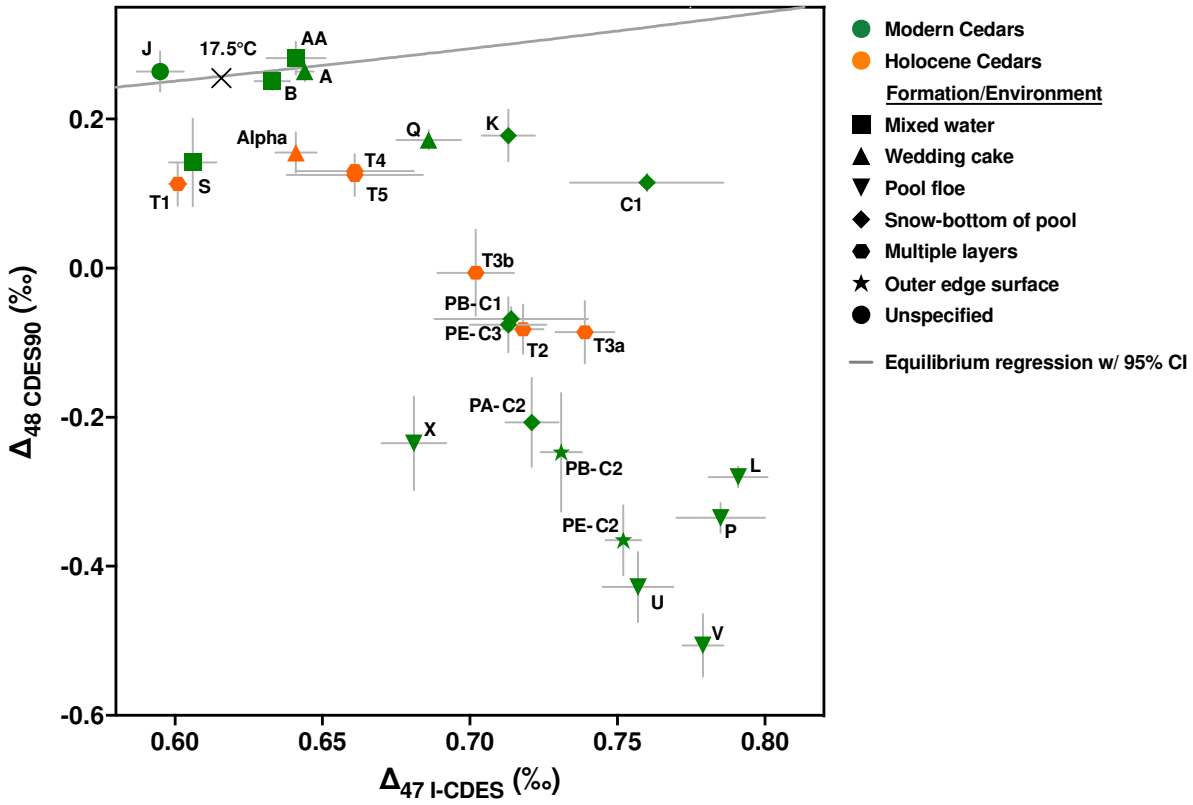


**Figure 3.** The $\Delta_{47}$ and $\Delta_{48}$ values for modern (green symbols) and Holocene (orange symbols) carbonate mineral samples at The Cedars. Results are compared to equilibrium values (gray line) (Lucarelli et al., 2023), with the average water temperature at The Cedars of 17.5±1 ºC (Morrill et al., 2013; Christensen et al., 2021) indicated (X symbol). The samples that exhibit the largest KIEs were primarily recovered from surface floes (pool floe, downward triangles). The samples that are within error (±1 SE) of equilibrium are from areas where surface and spring waters mix (squares), 1 wedding cake sample (triangle), and 1 sample from the GPS location from an unspecified formation (circle). A linear regression through all samples indicates a slope of -3.223±0.519. Error bars indicate ±1 SE.

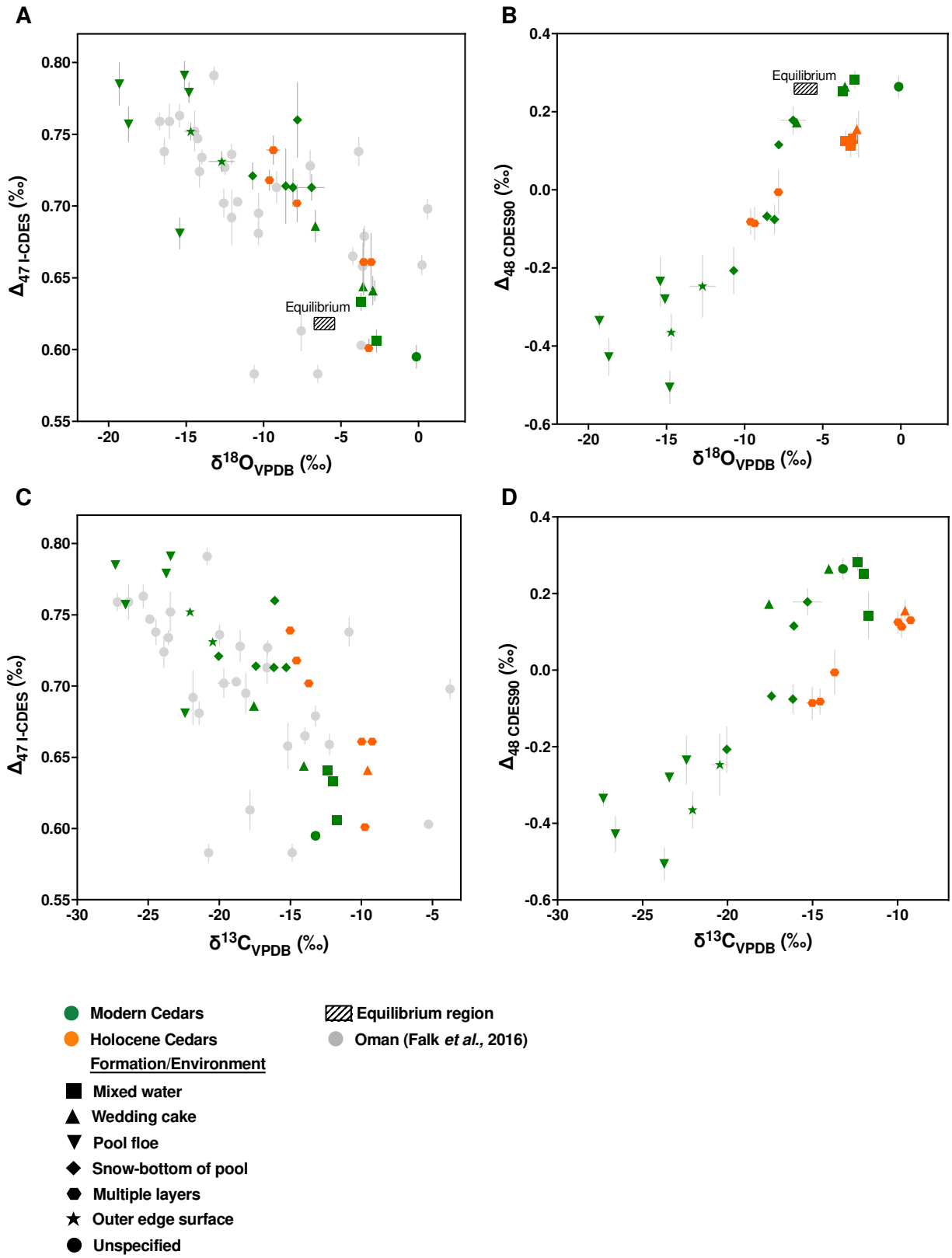
A
B
C
D
Equilibrium
Equilibrium
Δ47 I-CDES (‰)
Δ48 CDES90 (‰)
δ18OVPDB (‰)
δ13CVPDB (‰)
Modern Cedars
Holocene Cedars
Formation/Environment
Mixed water
Wedding cake
Pool floe
Snow-bottom of pool
Multiple layers
Outer edge surface
Unspecified
Equilibrium region
Oman (Falk et al., 2016)

804
805

**Figure 4.** Clumped isotope ($\Delta_{47}$, $\Delta_{48}$) versus bulk isotope ($\delta^{18}O$, $\delta^{13}C$) results of modern (green symbols) and Holocene (orange symbols) surface spring carbonate samples from The Cedars. Results are compared to calculated equilibrium values (striped rectangle) (Kim and O'Neil, 1997; Kim et al., 2007; Dietzel et al., 2009; Lucarelli et al., 2023). Panels A and C include data from carbonate veins precipitated from a peridotite body in Oman (gray cirlces) (Falk et al., 2016). **A)** $\Delta_{47}$ versus $\delta^{18}O$ values for The Cedars and Oman (Falk et al., 2016). A linear regression fit to The Cedars values yields a slope of -0.009±0.001, and a linear regression for the Cedars and Oman values yields a slope of -0.007±0.001. **B)** $\Delta_{48}$ versus $\delta^{18}O$ values for The Cedars. A linear regression fit to The Cedars values yields a slope of 0.041±0.003. **C)** $\Delta_{47}$ versus $\delta^{13}C$ values for The Cedars and Oman (Falk et al., 2016). A linear regression fit to The Cedars values yields a slope of -0.009±0.001, and a linear regression fit to The Cedars and Oman values yields a slope of -0.006±0.001. **D)** The $\Delta_{48}$ versus $\delta^{13}C$ values for The Cedars. A linear regression yields a slope of 0.038±0.005. The Oman $\Delta_{47}$ values were published in the CDES 25 reference frame and converted to the CDES 90 reference frame (which is comparable to the I-CDES reference frame used here) using an acid fractionation factor of 0.092‰ (Henkes et al., 2013). Equilibrium values were calculated using the average water temperature at The Cedars of 17.5 ºC (Morrill et al., 2013; Christiansen et al., 2021). Error bars indicate ±1 SE for clumped isotope values and ±1 SD for bulk isotope values.

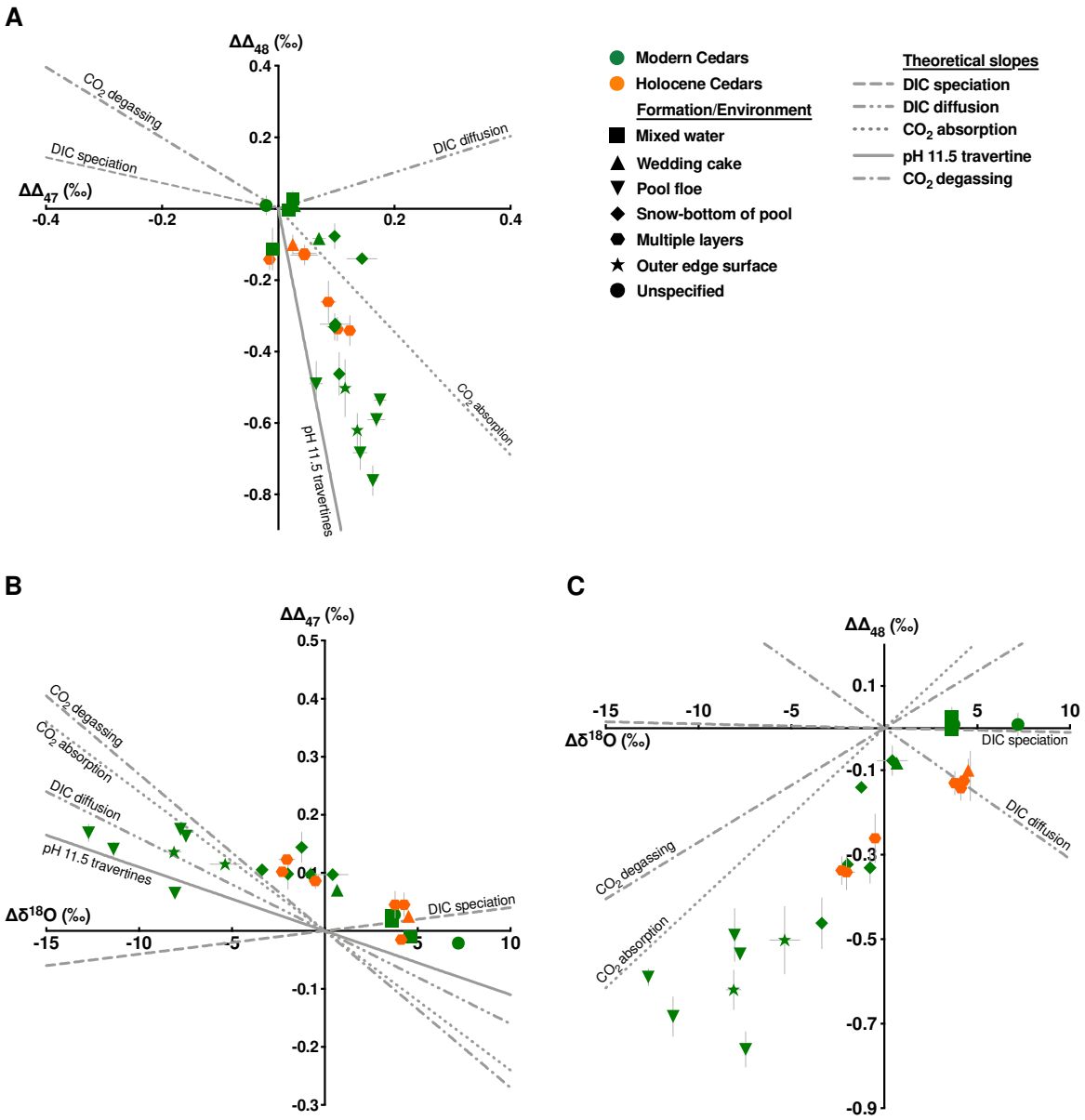


**Figure 5.** Extent of disequilibria in clumped ($\Delta_{47}$ and $\Delta_{48}$) and oxygen isotope ($\delta^{18}O$) values in the modern (green symbols) and Holocene (orange symbols) Cedars samples are shown with theoretically predicted kinetic slopes from multiple processes (gray lines) (Guo, 2020). The $\Delta\Delta_{47}$, $\Delta\Delta_{48}$, and $\Delta\delta^{18}O$ values were calculated by taking the difference between the measured values and the calculated equilibrium values (Kim and O'Neil, 1997; Kim et al., 2007; Lucarelli et al., 2023) for the average water temperature of The Cedars of 17.5 ºC (Morrill et al., 2013; Christiansen et al., 2021). **A)** $\Delta\Delta_{48}$ versus $\Delta\Delta_{47}$ values, with a linear regression slope of -3.223±0.519. **B)** $\Delta\Delta_{47}$ versus $\Delta\delta^{18}O$ values, with a linear regression slope of -0.009±0.001. **C)** $\Delta\Delta_{48}$ versus $\Delta\delta^{18}O$ values, with a linear regression slope of 0.040±0.003. Error bars indicate ±1 SE for clumped isotope values and ±1 SD for $\delta^{18}O$ values.

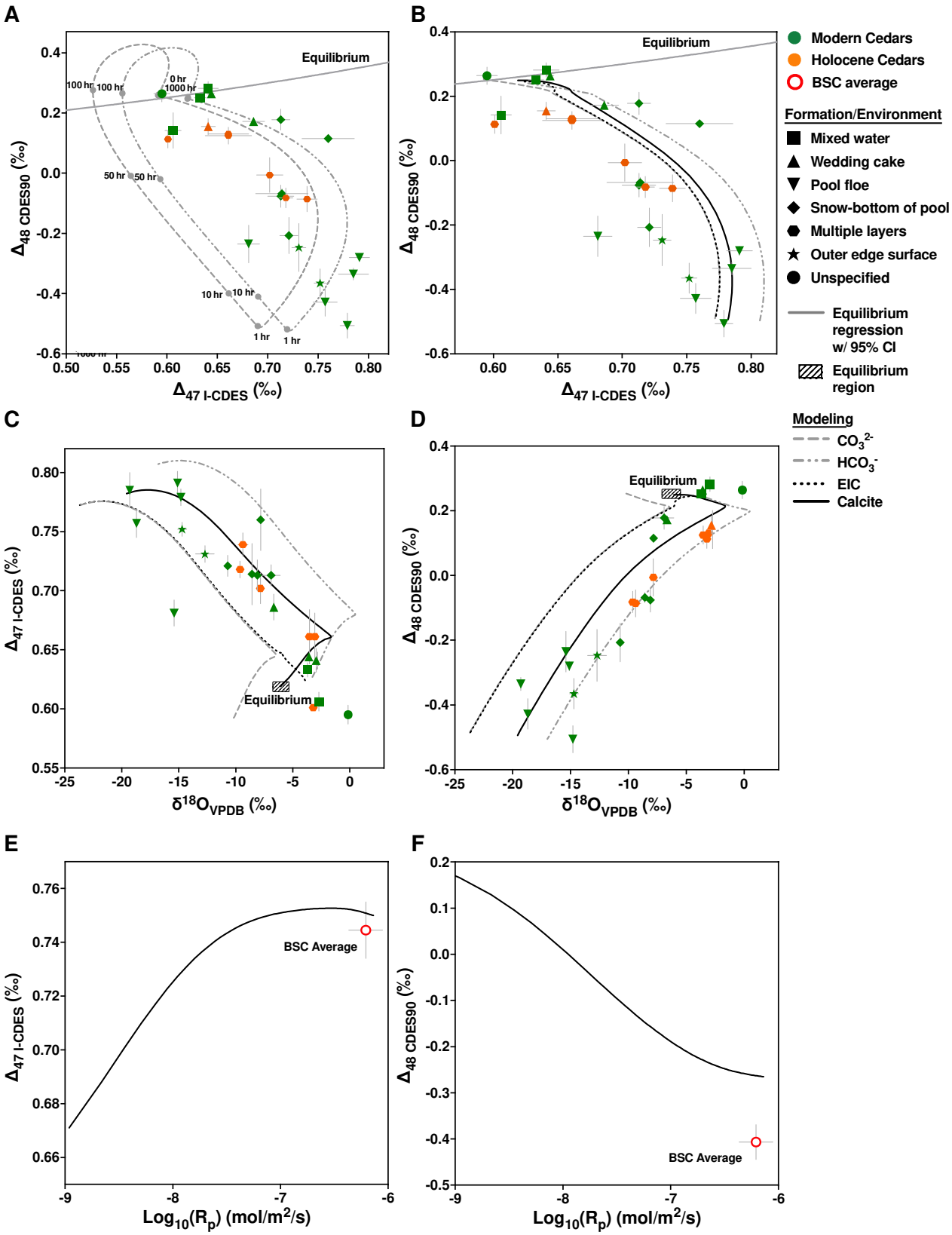
A
B
C
D
E
F
Equilibrium
0 hr
1000 hr
100 hr
50 hr
10 hr
1 hr
Δ48 CDES90 (‰)
Δ47 I-CDES (‰)
δ18OVPDB (‰)
Log10(Rp) (mol/m2/s)
BSC Average
Modern Cedars
Holocene Cedars
BSC average
Formation/Environment
Mixed water
Wedding cake
Pool floe
Snow-bottom of pool
Multiple layers
Outer edge surface
Unspecified
Equilibrium regression w/ 95% CI
Equilibrium region
Modeling
CO3 2-
HCO3 -
EIC
Calcite

854

**Figure 6.** Measured $\Delta_{47}$, $\Delta_{48}$, and $\delta^{18}O$ values from the modern (green symbols) and Holocene (orange symbols) Cedars samples compared to model predictions (gray and black curves), which were determined using code from the IsoDIC and COAD models. Also shown are the calculated equilibrium values based on the average water temperature at The Cedars of 17.5 ºC (gray line in panels A and B; striped rectangle in panels C and D) (Kim and O'Neil, 1997; Kim et al., 2007; Morrill et al., 2013; Christensen et al., 2021; Lucarelli et al., 2023). Panels E and F show the combined average $\Delta_{47}$ and $\Delta_{48}$ values (red circles) from samples collected at the BSC locality (samples X, U, V), with an apparent growth rate ($R_p$) of 4.8 x $10^{-7}$ to 8.0 x $10^{-7}$ mol $m^{-2}$ $s^{-1}$ (Christensen et al., 2021), compared to COAD model predicted values (black curves). **A)** Measured $\Delta_{47}$ and $\Delta_{48}$ values compared to IsoDIC model predicted values for $HCO_3^-$ and $CO_3^{-2}$ with the evolution time indicated. **B)** Measured $\Delta_{47}$ and $\Delta_{48}$ values with COAD model predicted values for calcite, $HCO_3^-$, $CO_3^{-2}$, and EIC. **C)** Measured $\Delta_{47}$ and $\delta^{18}O$ values with COAD model predicted values for calcite, $HCO_3^-$, $CO_3^{-2}$, and EIC. **D)** Measured $\Delta_{48}$ and $\delta^{18}O$ values with COAD model predicted values for calcite, $HCO_3^-$, $CO_3^{-2}$, and EIC. **E)** The measured and modeled $\Delta_{47}$ and $Log_{10}(R_p)$ values. The BSC average $\Delta_{47}$ value was determined to be 0.744±0.010‰. **F)** Measured and modeled $\Delta_{48}$ and $Log_{10}(R_p)$ values. The BSC average $\Delta_{48}$ value was determined to be -0.407±0.037‰. The IsoDIC and COAD models were based on the modern Cedars surface floe conditions. Error bars indicate ±1 SE for clumped isotope values and ±1 SD for $\delta^{18}O$ values.

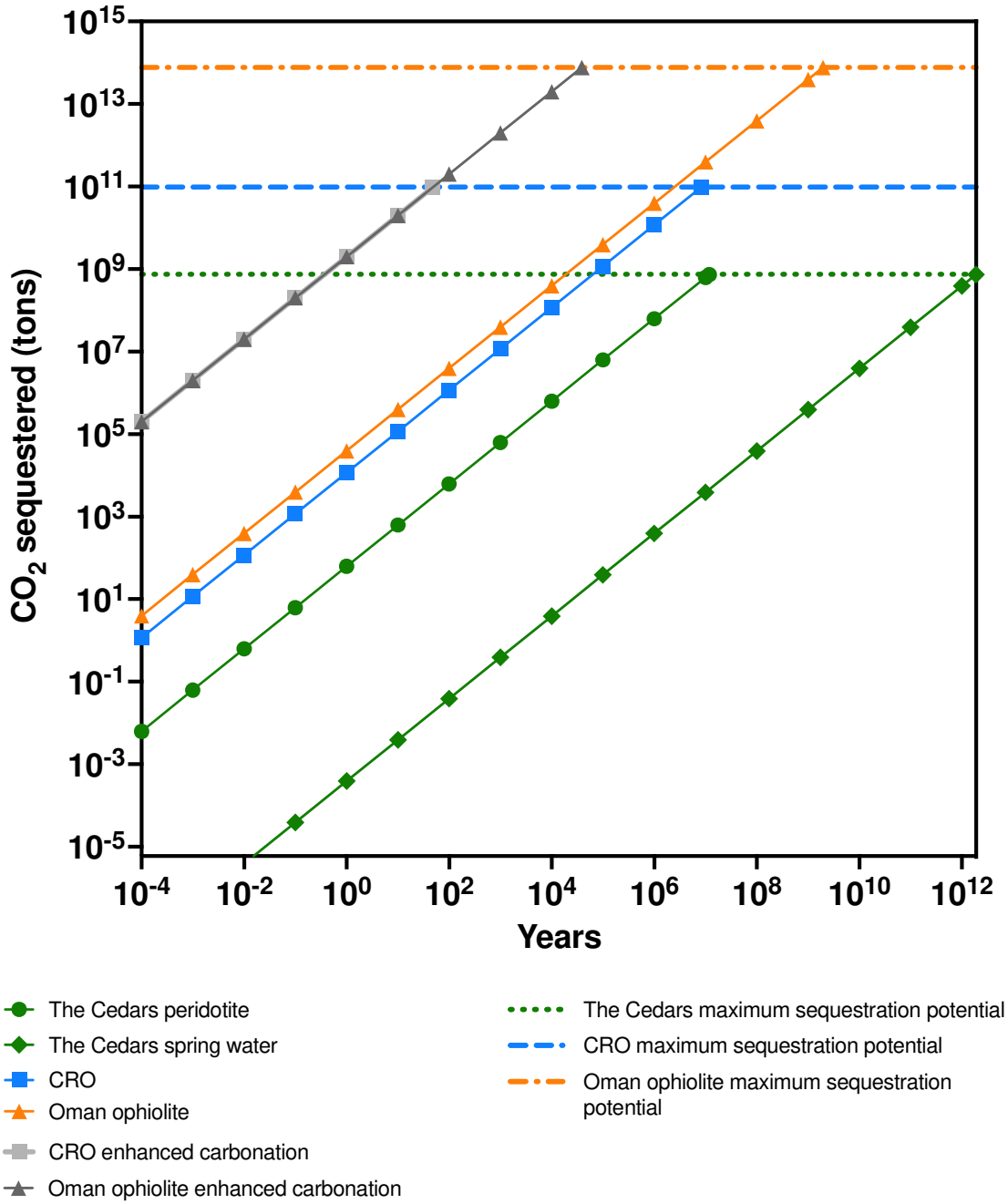


**Figure 7.** Calculations of natural rates of $CO_2$ sequestration in The Cedars peridotite (green circles), spring water at the site (green diamonds), the Coastal Range Ophiolite (CRO; blue squares), and the Oman ophiolite (orange triangles). The estimated maximum $CO_2$ sequestration potential was calculated to be ~$7.4 \times 10^8$ tons for The Cedars (green dotted line), ~$9.7 \times 10^{10}$ tons for the CRO (Carnevale, 2013; blue dashed line), and ~$7.7 \times 10^{13}$ tons for the Oman ophiolite (Kelemen and Matter, 2008; orange dash-dot line). The rate of mineral formation in The Cedars springs was measured by Christensen et al. (2021) and constrained here with our

888 dual clumped isotope measurements and modeled carbonate mineralization rates. In addition, the
889 $CO_2$ sequestered from enhanced *in situ* sequestration is shown for the CRO (gray squares) and
890 the Oman ophiolite (gray triangles), following methods from Kelemen and Matter (2008) for
891 enhanced geologic $CO_2$ sequestration in the Oman ophiolite of ~$2 \times 10^9$ tons of $CO_2$ sequestered
892 per year. For natural carbonation, we estimate that the sequestration potentials at The Cedars,
893 CRO, and Oman ophiolite would be reached after ~$8.2 \times 10^6$ years, ~$8.3 \times 10^6$ years, and ~$1.9 \times$
894 $10^9$ years, respectively. For enhanced *in situ* carbonation, the maximum sequestration potential at
895 the CRO and Oman Ophiolite could be reached in ~49 and ~38,500 years, respectively. All
896 calculated rates assume complete consumption of Mg, Ca, and Fe in the respective formations
897 (Kelemen and Matter, 2008; Matter and Kelemen, 2009; Carnevale, 2013), and consider the
898 ophiolite in Oman and the CRO to be ~30 % relict olivine (Kelemen and Matter, 2008;
899 Carnevale, 2013). The peridotite in The Cedars is ~70 % relict olivine (Coleman, 2000; Blake et
900 al., 2012; Morrill et al., 2013).
901

902 **Tables**
903

| Sample Name | Sample Composition | Location | Notes |
|---|---|---|---|
| A | Travertine | NS1 | Wedding Cake - Rim Formation |
| AA | Aragonite 91%; Calcite 1%; Brucite 8% | BSC | Mixed Water (BSC + Creek) |
| Alpha | Travertine | BSC | Wedding Cake - Rim Formation |
| B | Unspecified (Non-Travertine) | New Pool | Mixed Water (New Pool Spring + Creek) |
| C1 | Aragonite 86%; Calcite 7%; Brucite 7% | BSC | Snow - Bottom of Pool |
| J | Unspecified (Non-Travertine) | GPS | Unspecified |
| K | Aragonite 25%; Calcite 20%; Hydromagnesite 50%; Nitromagnesite 2%; Nesquehonite 3% | GPS | Snow - Bottom of Pool |
| L | Unspecified (Non-Travertine) | GPS | Pool Floe |
| P | Aragonite 78%; Calcite 18%; Brucite 4% | BSC | Pool Floe |
| PA-C2 | Unspecified (Non-Travertine) | BSC | Snow - Bottom of Pool |
| PB-C1 | Aragonite 86%; Calcite 7%; Brucite 7% | BSC | Snow - Bottom of Pool |
| PB-C2 | Aragonite 46%; Calcite 49%; Brucite 5% | BSC | Outer Edge Surface |
| PE-C2 | Aragonite 78%; Calcite 18%; Brucite 4% | BSC | Outer Edge Surface |
| PE-C3 | Unspecified (Non-Travertine) | BSC | Snow - Bottom of Pool |
| Q | Unspecified (Non-Travertine) | NS1 | Wedding Cake - Floe |
| S | Unspecified (Non-Travertine) | BSC | Mixed Water (BSC + Creek) |
| T1 | Travertine | BSC | Hand Sample - Multiple Layers |
| T2 | Travertine | BSC | Hand Sample - Multiple Layers |
| T3a | Travertine | BSC | Hand Sample - Multiple Layers |
| T3b | Travertine | BSC | Hand Sample - Multiple Layers |
| T4 | Travertine | BSC | Hand Sample - Multiple Layers |
| T5 | Travertine | BSC | Hand Sample - Multiple Layers |
| U | Unspecified (Non-Travertine) | BSC | Pool Floe |
| V | Unspecified (Non-Travertine) | BSC | Pool Floe |
| X | Unspecified (Non-Travertine) | BSC | Pool Floe |

904
905 **Table 1:** Sample information provided by Christensen et al. (2021).
906
907
908
909
910
911
912
913
914
915

| Sample Name | Number of Replicates | $\delta^{13}C_{VPDB}$ (‰) | 1 S.D. | $\delta^{18}O_{VPDB}$ (‰) | 1 S.D. | $\Delta\delta^{18}O$ (‰) | $\Delta_{47\ I\text{-}CDES}$ (‰) | 1 S.D. | 1 S.E. | $\Delta\Delta_{47}$ (‰) | $\Delta_{48\ CDES90}$ (‰) | 1 S.D. | 1 S.E. | $\Delta\Delta_{48}$ (‰) |
|---|---|---|---|---|---|---|---|---|---|---|---|---|---|---|

| | | | | | | | | | | | | | | |
|---|---|---|---|---|---|---|---|---|---|---|---|---|---|---|
| A | 3 | -14.1 | 0.0 | -3.6 | 0.1 | 3.8 | 0.644 | 0.005 | 0.003 | 0.028 | 0.264 | 0.022 | 0.013 | 0.009 |
| AA | 6 | -12.4 | 0.1 | -3.0 | 0.1 | 3.6 | 0.641 | 0.024 | 0.010 | 0.025 | 0.282 | 0.054 | 0.022 | 0.027 |
| Alpha | 6 | -9.6 | 0.1 | -2.8 | 0.1 | 4.5 | 0.641 | 0.016 | 0.007 | 0.025 | 0.155 | 0.066 | 0.027 | -0.100 |
| B | 3 | -12.0 | 0.0 | -3.7 | 0.0 | 3.6 | 0.633 | 0.010 | 0.006 | 0.017 | 0.251 | 0.021 | 0.012 | -0.004 |
| C1 | 4 | -16.1 | 0.1 | -7.8 | 0.2 | -1.2 | 0.760 | 0.051 | 0.026 | 0.144 | 0.115 | 0.025 | 0.012 | -0.140 |
| J | 4 | -13.2 | 0.0 | -0.1 | 0.2 | 7.2 | 0.595 | 0.015 | 0.008 | -0.021 | 0.264 | 0.054 | 0.027 | 0.009 |
| K | 9 | -15.3 | 0.8 | -6.9 | 0.8 | 0.4 | 0.713 | 0.027 | 0.009 | 0.097 | 0.178 | 0.104 | 0.035 | -0.077 |
| L | 4 | -23.4 | 0.1 | -15.1 | 0.1 | -7.8 | 0.791 | 0.020 | 0.010 | 0.175 | -0.280 | 0.027 | 0.014 | -0.535 |
| P | 5 | -27.3 | 0.0 | -19.3 | 0.0 | -12.7 | 0.785 | 0.033 | 0.015 | 0.169 | -0.335 | 0.045 | 0.020 | -0.590 |
| PA-C2 | 5 | -20.0 | 0.1 | -10.7 | 0.2 | -3.4 | 0.721 | 0.020 | 0.009 | 0.105 | -0.207 | 0.134 | 0.060 | -0.462 |
| PB-C1 | 3 | -17.4 | 0.0 | -8.6 | 0.1 | -2.0 | 0.714 | 0.045 | 0.026 | 0.098 | -0.068 | 0.028 | 0.016 | -0.323 |
| PB-C2 | 5 | -20.5 | 0.5 | -12.7 | 0.8 | -5.4 | 0.731 | 0.016 | 0.007 | 0.115 | -0.247 | 0.180 | 0.080 | -0.502 |
| PE-C2 | 11 | -22.1 | 0.2 | -14.7 | 0.4 | -8.1 | 0.752 | 0.021 | 0.006 | 0.136 | -0.365 | 0.157 | 0.047 | -0.620 |
| PE-C3 | 8 | -16.2 | 0.2 | -8.1 | 0.3 | -0.8 | 0.713 | 0.035 | 0.013 | 0.097 | -0.076 | 0.105 | 0.037 | -0.331 |
| Q | 5 | -17.6 | 0.1 | -6.7 | 0.1 | 0.7 | 0.686 | 0.025 | 0.011 | 0.070 | 0.172 | 0.029 | 0.013 | -0.083 |
| S | 3 | -11.7 | 0.0 | -2.7 | 0.1 | 4.6 | 0.606 | 0.014 | 0.008 | -0.010 | 0.142 | 0.102 | 0.059 | -0.113 |
| T1 | 6 | -9.8 | 0.1 | -3.2 | 0.2 | 4.1 | 0.601 | 0.007 | 0.003 | -0.015 | 0.113 | 0.072 | 0.029 | -0.142 |
| T2 | 13 | -14.6 | 0.2 | -9.6 | 0.3 | -2.3 | 0.718 | 0.024 | 0.007 | 0.102 | -0.082 | 0.119 | 0.033 | -0.337 |
| T3a | 13 | -15.0 | 0.4 | -9.4 | 0.4 | -2.0 | 0.739 | 0.036 | 0.010 | 0.123 | -0.086 | 0.153 | 0.042 | -0.341 |
| T3b | 3 | -13.7 | 0.2 | -7.8 | 0.1 | -0.5 | 0.702 | 0.023 | 0.013 | 0.086 | -0.006 | 0.100 | 0.058 | -0.261 |
| T4 | 3 | -10.0 | 0.1 | -3.5 | 0.1 | 3.8 | 0.661 | 0.039 | 0.023 | 0.045 | 0.125 | 0.049 | 0.028 | -0.130 |
| T5 | 3 | -9.2 | 0.0 | -3.1 | 0.0 | 4.3 | 0.661 | 0.035 | 0.020 | 0.045 | 0.130 | 0.013 | 0.007 | -0.125 |
| U | 5 | -26.6 | 0.0 | -18.7 | 0.1 | -11.4 | 0.757 | 0.028 | 0.012 | 0.141 | -0.428 | 0.104 | 0.047 | -0.683 |
| V | 11 | -23.7 | 0.1 | -14.8 | 0.1 | -7.5 | 0.779 | 0.023 | 0.007 | 0.163 | -0.506 | 0.139 | 0.042 | -0.761 |
| X | 7 | -22.4 | 0.1 | -15.4 | 0.1 | -8.1 | 0.681 | 0.029 | 0.011 | 0.065 | -0.235 | 0.167 | 0.063 | -0.490 |

**Table 2:** Clumped and bulk isotopic values for all samples measured in this study. The calculations to determine $\Delta\delta^{18}O$, $\Delta\Delta_{47}$, and $\Delta\Delta_{48}$ values were performed assuming equilibrium values for the average temperature at The Cedars of 17.5 $^{o}$C (Kim et al., 2007; Dietzel et al., 2009; Morrill et al., 2013; Christensen et al., 2021; Lucarelli et al., 2023).

## References


Affek, H. P., Bar-Matthews, M., Ayalon, A., Matthews, A., Eiler, J. M., 2008. Glacial/interglacial temperature variations in Soreq cave speleothems as recorded by 'clumped isotope' thermometry. Geochim. Cosmochim. Acta 72, 5351–5360.

Anderson, N. T., Kelson, J. R., Kele, S., Daëron, M., Bonifacie, M., Horita, J., Mackey, T. J., John, C. M., Kluge, T., Petschnig, P., Jost, A. B., Huntington, K. W., Bernasconi, S. M., Bergmann, K.D., 2021. A Unified Clumped Isotope Thermometer Calibration (0.5–1,100°C) Using Carbonate-Based Standardization. Geophys. Res. Lett. 48.

931 Bajnai, D., Guo, W., Spötl, C., Coplen, T.B., Methner, K., Löffler, N., Krsnik, E., Gischler, E.,
932 Hansen, M., Henkel, D., Price, G.D., Raddatz, J., Scholz, D., Fiebig, J., 2020. Dual
933 clumped isotope thermometry resolves kinetic biases in carbonate formation
934 temperatures. Nat. Commun. 11, 4005.

935 Barnes, I., O'Neil, J.R., 1969. The Relationship between Fluids in Some Fresh Alpine-Type
936 Ultramafics and Possible Modern Serpentinization, Western United States. Geol. Soc.
937 Am. Bull. 80, 1947.

938 Beck W.C., Grossman E.L., Morse J.W., 2005. Experimental studies of oxygen isotope
939 fractionation in the carbonic acid system at 15°, 25°, and 40°C. Geochim. Cosmochim.
940 Acta 69, 3493–3503.

941 Bernasconi, S.M., Daëron, M., Bergmann, K.D., Bonifacie, M., Meckler, A.N., Affek, H.P.,
942 Anderson, N., Bajnai, D., Barkan, E., Beverly, E., Blamart, D., Burgener, L., Calmels, D.,
943 Chaduteau, C., Clog, M., Davidheiser-Kroll, B., Davies, A., Dux, F., Eiler, J., Elliott, B.,
944 Fetrow, A.C., Fiebig, J., Goldberg, S., Hermoso, M., Huntington, K.W., Hyland, E.,
945 Ingalls, M., Jaggi, M., John, C.M., Jost, A.B., Katz, S., Kelson, J., Kluge, T., Kocken, I.
946 J., Laskar, A., Leutert, T.J., Liang, D., Lucarelli, J., Mackey, T.J., Mangenot, X.,
947 Meinicke, N., Modestou, S.E., Müller, I.A., Murray, S., Neary, A., Packard, N., Passey,
948 B.H., Pelletier, E., Petersen, S., Piasecki, A., Schauer, A., Snell, K.E., Swart, P.K.,
949 Tripati, A., Upadhyay, D., Vennemann, T., Winkelstern, I., Yarian, D., Yoshida, N.,
950 Zhang, N., Ziegler M., 2021. InterCarb: A Community Effort to Improve Interlaboratory
951 Standardization of the Carbonate Clumped Isotope Thermometer Using Carbonate
952 Standards. Geochem. Geophys. Geosyst. 22(5).

953 Bernasconi, S.M., Müller, I.A., Bergmann, K.D., Breitenbach, S.F.M., Fernandez, A., Hodell,
954 D.A., Jaggi, M., Meckler, A.N., Millan, I., Ziegler M., 2018. Reducing Uncertainties in
955 Carbonate Clumped Isotope Analysis Through Consistent Carbonate-Based
956 Standardization. Geochem. Geophys. Geosyst. 19, 2895–2914.

957 Blake, M.C., Bailey, E.H., Wentworth, C.M., 2012. The Cedars Ultramafic Mass, Sonoma
958 County, California. USGS Open-File Rep. 2012–1164, 1–16.

959 Brand W. A., Assonov S. S. and Coplen T. B., 2010. Correction for the $^{17}O$ interference in $\delta^{13}C$
960 measurements when analyzing $CO_2$ with stable isotope mass spectrometry (IUPAC
961 Technical Report). Pure Appl. Chem. 82, 1719–1733.

962 Bruni, J., Canepa, M., Chiodini, G., Cioni, R., Cipolli, F., Longinelli, A., Marini, L., Ottonello,
963 G., Vetuschi Zuccolini M., 2002. Irreversible water-rock mass transfer accompanying the
964 generation of the neutral, Mg-$HCO_3$ and high-pH, Ca-OC spring waters of the Genova
965 province, Italy. Appl. Geochem. 17, 455–474.

966 Carnevale, D.C., 2013. Carbon sequestration potential of the Coast Range Ophiolite in
967 California., University of Rhode Island ProQuest Dissertations Publishing.

968 Chen, S., Gagnon, A.C., Adkins J.F., 2018. Carbonic anhydrase, coral calcification and a new
969 model of stable isotope vital effects. Geochim. Cosmochim. Acta 236, 179–197.

970 Christensen, J.N., Watkins, J.M., Devriendt, L.S., DePaolo, D.J., Conrad, M.E., Voltolini, M.,
971 Yang, W. and Dong, W., 2021. Isotopic fractionation accompanying $CO_2$ hydroxylation
972 and carbonate precipitation from high pH waters at The Cedars, California, USA.
973 Geochim. Cosmochim. Acta 301, 91–115.

974 Cipolli, F., Gambardella, B., Marini, L., Ottonello, G., Vetuschi Zuccolini, M., 2004.
975 Geochemistry of high-pH waters from serpentinites of the Gruppo di Voltri (Genova,
976 Italy) and reaction path modeling of $CO_2$ sequestration in serpentinite aquifers. Appl.
977 Geochem. 19, 787–802.

978 Coleman, R.G., 2004. Geologic Nature of the Jasper Ridge Biological Preserve, San Francisco
979 Peninsula, California. Int. Geol. Rev. 46, 629–637.

980 Coleman R. G., 2000. Prospecting for ophiolites along the California continental margin. Geol.
981 Soc. Am. Special Paper 349, 351–364.

982 Daëron, M., Blamart, D., Peral, M., Affek, H., P., 2016. Absolute isotopic abundance ratios and
983 the accuracy of $\Delta_{47}$ measurements. Chem. Geol. 442, 83–96.

984 Defliese, W.F., Lohmann, K.C., 2015. Non-linear mixing effects on mass-47 $CO_2$ clumped
985 isotope thermometry: Patterns and implications: Non-linear mixing effects on mass-47
986 clumped isotopes. Rapid Commun. Mass Spectrom. 29, 901–909.

987 Dennis, K.J., Affek, H.P., Passey, B.H., Schrag, D.P., Eiler, J.M., 2011 Defining an absolute
988 reference frame for 'clumped' isotope studies of $CO_2$. Geochim. Cosmochim. Acta 75,
989 7117–7131.

990 Devriendt, LS., Watkins, J. M., McGregor, H.V., 2017. Oxygen isotope fractionation in the
991 $CaCO_3$-DIC-$H_2O$ system. Geochim. Cosmochim. Acta 214, 115–142.

992 Dietzel, M., Tang, J., Leis, A., Köhler, S.J., 2009. Oxygen isotopic fractionation during inorganic
993 calcite precipitation — Effects of temperature, precipitation rate and pH. Chem. Geol.
994 268, 107–115.

995 Drohan, P.J., Brittingham, M., 2012. Topographic and Soil Constraints to Shale-Gas
996 Development in the Northcentral Appalachians. Soil Sci. Soc. Am. J. 76, 1696–1706.

997 Eiler, J.M., 2007. "Clumped-isotope" geochemistry—The study of naturally-occurring, multiply-
998 substituted isotopologues. Earth Planet. Sci. Lett. 262, 309–327.

999 Eiler, J. M., Schauble, E., 2004. $^{18}O^{13}C^{16}O$ in Earth's atmosphere. Geochim. Cosmochim. Acta
1000 68, 4767–4777.

1001 Falk, E.S., Guo, W., Paukert, A.N., Matter, J.M., Mervine, E.M., and Kelemen, P.B., 2016.
1002 Controls on the stable isotope compositions of travertine from hyperalkaline springs in
1003 Oman: Insights from clumped isotope measurements. Geochim. Cosmochim. Acta 192,
1004 1–28.

1005 Fiebig, J., Bajnai, D., Löffler N., Methner, K., Krsnik, E., Mulch, A., Hofmann, S., 2019.
1006 Combined high-precision $\Delta_{48}$ and $\Delta_{47}$ analysis of carbonates. Chem. Geol. 522, 186–191.

1007 Fiebig, J., Daëron, M., Bernecker, M., Guo, W., Schneider, G., Boch, R., Bernasconi, S.M.,
1008 Jautzy, J. and Dietzel, M., 2021. Calibration of the dual clumped isotope thermometer for
1009 carbonates. Geochim. Cosmochim. Acta, S0016703721004208.

1010 García del Real, P., Maher, K., Kluge, T., Bird, D.K., Brown, G.E. and John, C.M., 2016.
1011 Clumped-isotope thermometry of magnesium carbonates in ultramafic rocks. Geochim.
1012 Cosmochim. Acta 193, 222–250.

1013 Ghosh, P., Adkins, J., Affek, H., Balta B., Guo, W., Schauble, E.A., Schrag, D., Eiler, J.M..
1014 2006. $^{13}C$–$^{18}O$ bonds in carbonate minerals: A new kind of paleothermometer. Geochim.
1015 Cosmochim. Acta 70, 1439–1456.

1016 Guo, W., 2020. Kinetic clumped isotope fractionation in the DIC-$H_2O$-$CO_2$ system: Patterns,
1017 controls, and implications. Geochim. Cosmochim. Acta 268, 230–257.

1018 Guo, W., Mosenfelder, J.L., Goddard, W.A., and Eiler, J.M., 2009. Isotopic fractionations
1019 associated with phosphoric acid digestion of carbonate minerals: Insights from first-
1020 principles theoretical modeling and clumped isotope measurements. Geochim.
1021 Cosmochim. Acta 73, 7203–7225.

1022 Guo, W., Zhou, C., 2019. Patterns and controls of disequilibrium isotope effects in speleothems:
1023 Insights from an isotope-enabled diffusion-reaction model and implications for
1024 quantitative thermometry. Geochim. Cosmochim. Acta 267, 196–226.

1025 Hendy, C. H., 1971. The isotopic geochemistry of speleothems—I. The calculation of the effects
1026 of different modes of formation on the isotopic composition of speleothems and their
1027 applicability as palaeoclimatic indicators. Geochim. Cosmochim. Acta 35, 801–824.

1028 Henkes, G.A., Passey, B.H., Wanamaker, A.D., Grossman, E.L., Ambrose, W.G., Carroll, M.L.,
1029 2013. Carbonate clumped isotope compositions of modern marine mollusk and
1030 brachiopod shells. Geochim. Cosmochim. Acta 106, 307–325.

1031 Hill, P.S., Schauble, E.A., Tripati, A., 2020. Theoretical constraints on the effects of added
1032 cations on clumped, oxygen, and carbon isotope signatures of dissolved inorganic carbon
1033 species and minerals. Geochim. Cosmochim. Acta 269, 496–539.

1034 Hill, P.S., Tripati, A.K., Schauble, E.A., 2014. Theoretical constraints on the effects of pH,
1035 salinity, and temperature on clumped isotope signatures of dissolved inorganic carbon
1036 species and precipitating carbonate minerals. Geochim. Cosmochim. Acta 125, 610–652.

1037 Holzman, D.C., 2011. Methane Found in Well Water Near Fracking Sites. Environ. Health
1038 Perspect. 119.

John, C.M., Bowen, D., 2016. Community software for challenging isotope analysis: First applications of 'Easotope' to clumped isotopes: Community software for challenging isotope analysis. Rapid Commun. Mass Spectrom. 30, 2285–2300.

Kastrinakis, A., Skliros, V., Tsakiridis, P., Perraki, M., 2021. $CO_2$-Mineralised Nesquehonite: A New "Green" Building Material. In International Conference on Raw Materials and Circular Economy RawMat 2021. MDPI. p. 60.

Kelemen, P.B., Matter, J., 2008), In situ carbonation of peridotite for $CO_2$ storage. Proc. Natl. Acad. Sci. 105, 17295–17300.

Kelemen, P.B., Matter, J., Streit, E.E., Rudge, J.F., Curry, W.B., Blusztajn, J., 2011. Rates and Mechanisms of Mineral Carbonation in Peridotite: Natural Processes and Recipes for Enhanced, in situ $CO_2$ Capture and Storage. Annu. Rev. Earth Planet. Sci. 39, 545–576.

Kim, S.-T., O'Neil, J.R., 1997. Equilibrium and nonequilibrium oxygen isotope effects in synthetic carbonates. Geochim. Cosmochim. Acta 61, 3461–3475.

Kim, S.-T., O'Neil, J.R., Hillaire-Marcel, C., Mucci, A., 2007. Oxygen isotope fractionation between synthetic aragonite and water: Influence of temperature and $Mg^{2+}$ concentration. Geochim. Cosmochim. Acta 71, 4704–4715.

Kiviat, E., 2013. Risks to biodiversity from hydraulic fracturing for natural gas in the Marcellus and Utica shales: Hydraulic fracturing and biodiversity. Ann. N. Y. Acad. Sci. 1286, 1–14.

Lerman, A., Stumm, W., 1989. $CO_2$ storage and alkalinity trends in lakes. Water Res. 23, 139–146.

Liu, Z., Deng, Z., Davis, S.J., Giron, C. Ciais, P., 2022. Monitoring global carbon emissions in 2021. Nat. Rev. Earth Environ. 3, 217–219.

Lívanský, K., 1982. Effect of temperature and pH on absorption of carbon dioxide by a free level of mixed solutions of some buffers. Folia Microbiol. (Praha) 27, 55–59.

Lucarelli, J.K., Carroll, H.M., Ulrich, R.N., Elliott, B.M., Coplen, T.B., Eagle, R.A., Tripati, A., 2023. Equilibrated Gas and Carbonate Standard-Derived Dual ($\Delta_{47}$ and $\Delta_{48}$) Clumped Isotope Values. Geochem. Geophys. Geosyst. 24(2).

Matter, J.M., Kelemen, P.B., 2009. Permanent storage of carbon dioxide in geological reservoirs by mineral carbonation. Nat. Geosci. 2, 837–841.

McConnaughey, T., 1989. $^{13}C$ and $^{18}O$ isotopic disequilibrium in biological carbonates: II. In vitro simulation of kinetic isotope effects. Geochim. Cosmochim. Acta 53, 163–171.

McDermott, F., Atkinson, T.C., Fairchild, I.J., Baldini, L.M., Mattey, D.P., 2011. A first evaluation of the spatial gradients in $\delta^{18}O$ recorded by European Holocene speleothems. Glob. Planet. Change 79, 275–287.

Moody, J. B., 1976. Serpentinization: a review. Lithos 9, 125–138.

Morrill, P.L., Kuenen, J.G., Johnson, O.J., Suzuki, S., Rietze, A., Sessions, A.L., Fogel, M.L., Nealson, K. H., 2013. Geochemistry and geobiology of a present-day serpentinization site in California: The Cedars. Geochim. Cosmochim. Acta 109, 222–240.

de Obeso, J.C., Kelemen, P.B., 2018. Fluid rock interactions on residual mantle peridotites overlain by shallow oceanic limestones: Insights from Wadi Fins, Sultanate of Oman. Chem. Geol. 498, 139–149.

Passey, B.H., Levin, N.E., Cerling, T.E., Brown, F.H., Eiler, J.M., 2010. High-temperature environments of human evolution in East Africa based on bond ordering in paleosol carbonates. Proc. Natl. Acad. Sci. 107, 11245–11249.

Power, I.M., Wilson, S.A., Dipple, G., M., 2013. Serpentinite Carbonation for $CO_2$ Sequestration. Elements 9, 115–121.

Power, I. M., Wilson, S.A., Small, D.P., Dipple, G.M., Wan, W., Southam, G., 201. Microbially Mediated Mineral Carbonation: Roles of Phototrophy and Heterotrophy. Environ. Sci. Technol. 45, 9061–9068.

Saenger, C., Affek, H.P., Felis, T., Thiagarajan, N., Lough, J.M., Holcomb, M., 2012. Carbonate clumped isotope variability in shallow water corals: Temperature dependence and growth-related vital effects. Geochim. Cosmochim. Acta 99, 224–242.

Schauble, E.A., Ghosh, P., Eiler, J.M., 2006. Preferential formation of $^{13}C$–$^{18}O$ bonds in carbonate minerals, estimated using first-principles lattice dynamics. Geochim. Cosmochim. Acta 70, 2510–2529.

Schefer, J., Grube, M., 1995. Low temperature structure of magnesium nitrate hexahydrate, Mg $(NO_3)_2 \cdot 6H_2O$: A neutron diffraction study at 173 K. Mater. Res. Bull. 30, 1235–1241.

Sleep, N. H., Meibom, A., Fridriksson, Th., Coleman, R.G., Bird, D.K., 2004. $H_2$-rich fluids from serpentinization: Geochemical and biotic implications. Proc. Natl. Acad. Sci. 101, 12818–12823.

Spooner, P. T., Guo, W., Robinson, L.F., Thiagarajan, N., Hendry, K.R., Rosenheim, B.E., Leng M.J., 2016. Clumped isotope composition of cold-water corals: A role for vital effects? Geochim. Cosmochim. Acta 179, 123–141.

Suzuki, S., Ishii, S., Hoshino, T., Rietze, A., Tenney, A., Morrill, P.L., Inagaki, F., Kuenen, J.G., Nealson, K.H., 2017. Unusual metabolic diversity of hyperalkaliphilic microbial communities associated with subterranean serpentinization at the Cedars. ISME J. 11, 2584–2598.

Swart, P.K., Lu, C., Moore, E.W., Smith, M.E., Murray, S.T., Staudigel, P.T., 2021, A calibration equation between $\Delta_{48}$ values of carbonate and temperature. Rapid Commun. Mass Spectrom. 35.

1110 Tang, J., Dietzel, M., Fernandez, A., Tripati, A.K., Rosenheim, B.E., 2014. Evaluation of kinetic
1111 effects on clumped isotope fractionation ($\Delta_{47}$) during inorganic calcite precipitation.
1112 Geochim. Cosmochim. Acta 134, 120–136.

1113 Thiagarajan, N., Adkins, J., Eiler, J., 2011. Carbonate clumped isotope thermometry of deep-sea
1114 corals and implications for vital effects. Geochim. Cosmochim. Acta 75, 4416–4425.

1115 Tripati, A.K., Hill, P.S., Eagle, R.A., Mosenfelder, J.L., Tang, J., Schauble, E.A., Eiler, J.M.,
1116 Zeebe, R.E., Uchikawa, J., Coplen, T.B., Ries, J.B., Henry, D., 2015. Beyond
1117 temperature: Clumped isotope signatures in dissolved inorganic carbon species and the
1118 influence of solution chemistry on carbonate mineral composition. Geochim.
1119 Cosmochim. Acta 166, 344–371.

1120 Uchikawa, J., Chen, S., Eiler, J.M., Adkins, J.F., Zeebe, R., E., 2021. Trajectory and timescale of
1121 oxygen and clumped isotope equilibration in the dissolved carbonate system under
1122 normal and enzymatically-catalyzed conditions at 25 °C. Geochim. Cosmochim. Acta
1123 314, 313–333.

1124 Uchikawa, J., Zeebe, R.E., 2012. The effect of carbonic anhydrase on the kinetics and
1125 equilibrium of the oxygen isotope exchange in the $CO_2$–$H_2O$ system: Implications for
1126 $\delta^{18}O$ vital effects in biogenic carbonates. Geochim. Cosmochim. Acta 95, 15–34.

1127 United Nations Environment Programme, 2019. Emissions Gap Report 2018.

1128 Upadhyay, D., Lucarelli, J., Arnold, A., Flores, R., Bricker, H., Ulrich, R.N., Jesmok, G., Santi,
1129 L., Defliese, W., Eagle, R.A., Carroll, H.M., Bateman, J.B., Petryshyn, V., Loyd, S.J.,
1130 Tang, J., Priyadarshi, A., Elliott, B., Tripati, A., 2021. Carbonate clumped isotope
1131 analysis ($\Delta_{47}$) of 21 carbonate standards determined via gas-source isotope-ratio mass
1132 spectrometry on four instrumental configurations using carbonate-based standardization
1133 and multiyear data sets. Rapid Commun. Mass Spectrom. 35.

1134 Usdowski, E., Michaelis, J., Boettcher, M., Hoefs, J., 1991. Factors for the oxygen isotope
1135 equilibrium fractionation between aqueous and gaseous $CO_2$, carbonic acid, bicarbonate,
1136 carbonate, and water (19°C). Z. Phys. Chem.-Int. J. Res. Phys. Chem. Chem. Phys. 170,
1137 237–249.

1138 Watkins, J., Devriendt, L., 2022. A combined model for kinetic clumped isotope effects in the
1139 $CaCO_3$-DIC-$H_2O$ system., Geochem. Geophys. Geosyst. 23(8).

1140 Watkins, J. M., Hunt, J. D., 2015. A process-based model for non-equilibrium clumped isotope
1141 effects in carbonates. Earth Planet. Sci. Lett. 432, 152–165.

1142 Weise, A., Kluge, T., 2020. Isotope exchange rates in dissolved inorganic carbon between 40 °C
1143 and 90 °C. Geochim. Cosmochim. Acta 268, 56–72.

1144 Zedef, V., Russell, M.J., Fallick, A.E., Hall, A.J., 2000. Genesis of Vein Stockwork and
1145 Sedimentary Magnesite and Hydromagnesite Deposits in the Ultramafic Terranes of
1146 Southwestern Turkey: A Stable Isotope Study. Econ. Geol. 95, 429–445.

1147 Zeebe, R.E., Wolf-Gladrow, D.A., 2001. $CO_2$ in seawater: equilibrium, kinetics, isotopes.
1148 Elsevier, Amsterdam, New York.

1149